FLORIDA STATE UNIVERSITY

COLLEGE OF ARTS AND SCIENCES

CHARACTERIZING THE NORTHERN AUSTRALIAN RAINY SEASON FROM THE LARGE-SCALE TO THE LOCAL SCALE IN THE CURRENT AND THE FUTURE CLIMATE

By

JOHN UEHLING

A dissertation submitted to the
Department of Earth, Ocean, and Atmospheric Science
in partial fulfillment of the
requirements for the degree of
Doctor of Philosophy in Meteorology

2021

John Uehling defended this dissertation on October 28, 2021.
The members of the supervisory committee were:

Vasubandhu Misra
Professor Directing Dissertation

Sachin Shanbhag
University Representative

Allison Wing
Committee Member

Alyssa Atwood
Committee Member

Guosheng Liu
Committee Member

Jeffery Chagnon
Committee Member

The Graduate School has verified and approved the above-named committee members, and certifies that the dissertation has been approved in accordance with university requirements.

TABLE OF CONTENTS

LIST OF TABLES

LIST OF FIGURES

ABSTRACT

The northern Australian rainy season is part of the Asian-Australian monsoon system and occurs during the Austral summer across the northern regions of the continent. The Australian monsoon is responsible for most of the annual rainfall budget for the region, thus having a comprehensive understanding of the rainy season is of vital importance for socio-economic and environmental considerations.

In this dissertation, we objectively define onset and demise of the rainy season, locally (at a given grid point of the observed rainfall analysis) from the definition of aggregate northern Australian rainy season. This definition allows to account for the variations of the length of the rainy season in addition to the variations in the daily rain rate, which together contribute to the seasonal variability of the rainfall. We further analyze the variations of the local onset and demise dates, length and seasonal rainfall anomaly of the northern Australian rainy season from the intraseasonal to the secular scales. The results from this study uniquely highlight the spatial heterogeneity of the seasonal evolution of the rainy season and its variability. The spatial distribution of the frequency of local demise of NARS during the various phases of the ISO exhibit coherent areas of high frequency during dry phases of ISO around the Gulf of Carpentaria.

This study then examines the fidelity of the Coupled Model Intercomparison Project version 6 (CMIP6) models from their historical simulations to simulate these observed features. The analyzed CMIP6 simulations over the northern Australian region have shown promise in some of the features of the rainy season that we identify in this study. For example, the onset and the demise dates of the rainy season are reasonable and its association with El Niño and the Southern Oscillation is also verifiable. The CMIP6 model projections for Shared Socio-economic Pathway SSP126 (or green pathway) and the high emission SSP585 (or fossil-fueled pathway) scenarios towards the end of the 21st century were independently analyzed to show the impacts of anthropogenic climate change on the northern Australian region. Our broad conclusion from this analysis is that the impact of the anthropogenic change on the northern Australian rainy season is statistically insignificant. However, it should be noted that these CMIP6 models displayed poor fidelity in simulating the observed linear trends of the 20th century northern Australian rainy season.

CHAPTER 1

INTRODUCTION

The northern Australian monsoon has been an area of increased interest in recent years, due to increases in population in the region and the importance of the rainfall to agriculture in the largely arid continent (Anwar et al. 2007; Qureshi et al. 2013). Monsoon rains are the primary precipitation producers in northern Australia, and thus it is of utmost importance to understand and predict them. Recent studies have indicated that the climatology of the northern Australian rainy season (NARS; which mostly overlaps with the monsoon season) has been changing, perhaps as a result of anthropogenic climate change (Brown et al. 2016; Narsay et al. 2020; Uehling and Misra, 2020).

There have been numerous studies that have been used and cited to describe the length and the climatology of the northern Australian monsoon and of the NARS (Troup 1961; McBride 1983, 1986; Nicholls 1984; Wang 2003; Lisonbee 2019; Uehling and Misra 2020). A subtle but important distinction is made between the two seasons, with the NARS focusing on the seasonal cycle of precipitation, while the Australian monsoon season additionally considers the atmospheric circulation field as well. This study focuses on a methodology based purely on rainfall to diagnose changes in length of the season that has previously been used over India (Noska and Misra, 2016; Misra et al. 2017) as well as Australia (Uehling and Misra 2020). This rainfall-derived definition for the NARS allows for a comprehensive and robust definition. In contrast to the previous study of Uehling and Misra (2020), this effort attempts to define the NARS with higher granularity so that the spatial and temporal variability at finer resolution can be resolved.

Having the climatological data surrounding the northern Australian monsoon and rainy season is an important starting point to gather a more complete understanding of the monsoon, by

allowing us to understand not only how the monsoon has behaved historically, but also how it might change moving forward. However, there are numerous other important and interesting areas of research that have been explored. Intraseasonal oscillations (ISOs) are important features of monsoonal rains (Webster et al. 1998; Annamalai and Slingo 2001; Goswami and Ajaya Mohan 2001). Intraseasonal cycles in the 20-90 day time scale are periods of more active or less active precipitation phases that occur at irregular intervals throughout a monsoon season (Webster et al. 1998; Annamalai and Slingo 2001; Goswami and Ajaya Mohan 2001; Goswami 2005; Chakraborty and Nanjundiah 2012; Karmakar 2016). These oscillations have been studied in great detail over the Indian subcontinent and understanding them has been vitally important due to the socio-economic implications of their existence (Karmakar 2016). These intraseasonal oscillations have been shown to influence the timing of the onset and demise of the monsoon over the Indian subcontinent (Karmakar 2016). During the peak (highest rainfall phases) of the ISOs, the majority of local onsets occurred during the Indian monsoon (Karmakar, 2016). Similarly, during the dry phases of the ISOs, there was a preference for the demise of the monsoon to occur. The strong relationship between the ISOs and the local onset and demise motivates a similar analysis of ISOs influence of the onset and demise of the northern Australian rainy season.

Despite the importance of understanding these ISOs, there has been comparatively limited research done with regards to the northern Australian monsoon (Meehl et al. 2020; Narsay et al. 2017). To gain a more complete understanding of the sub-seasonal variations of the northern Australian monsoon, a Multichannel Singular Spectrum Analysis (MSSA) was performed. The MSSA technique is used to understand the unknown or partially known dynamics of a given dynamical system (Broomhead and King 1986). MSSA can systematically extract the coherent

spatio-temporal signals within a given time series. (Allen and Robertson, 2006; Ghil et al. 2002; Moron et al. 2012; Karmakar 2016).

Using the MSSA technique, the dynamics of the northern Australian intraseasonal oscillations can be further understood. It is important to understand what global features might have teleconnections with the NARS, and thus the effects of the Madden-Julian oscillation (a boreal winter intraseasonal oscillation) on the onset and the demise of the monsoon are also analyzed.

Additionally, climate models were utilized to analyze potential anthropogenic forcing on the northern Australian monsoon season. Taking the analysis methods discussed previously to determine the climatology of the NARS, it becomes an obvious step to study how these features might change in a future climate under different emission scenarios. The newly released CMIP6 models provide an avenue to assess future projections that can be used to analyze how the dynamics of the NARS might change with time

There have been numerous studies looking at the impact of climate change on northern Australian monsoon season and the NARS (Narsay wt al 2020, Brown et al 2016, Wang et al 2014). Previous attempts to study the region using historical runs from the Coupled Model Intercomparison Project Phase 5 (CMIP5) yielded inconclusive results, with different models showing either increasing or decreasing trends in rainfall (Narsay et al. 2020).

With the recent release of the Coupled Model Intercomparison Project Phase 6 (CMIP6), there is an opportunity to gain further insight into the NARS and how it might respond to a changing climate. There have already been a few recent studies analyzing the northern Australian monsoon using the CMIP6 models, with the goal being to determine the potential impact of climate change on the region.

One study found disagreement in the CMIP6 models about potential climate change impacts over northern Australia (Narsay et al. 2020). It was found that though the overall variance between the models in CMIP6 was reduced when compared to CMIP5, the models continued to show differences in both magnitude and direction of change of the monsoon (Narsay et al. 2020). What this suggests is that the CMIP6 models still have not been able to discern whether or not anthropogenic forcing will lead to an increase in precipitation or a decrease in precipitation over the northern Australian domain. An interesting finding was also that it appears that the changes in the western Pacific Ocean is not strongly connected to the northern Australian precipitation changes (Narsay et al. 2020). Overall, there appears to be a disagreement on exactly how much, and in what direction, precipitation changes will occur during the northern Australian monsoon season because of anthropogenic climate change.

As mentioned previously, there have been several studies that have attempted to answer the question of whether anthropogenic climate change will lead to precipitation changes over the Australian domain. Brown et al. (2016) analyzed multi-model mean projections for the Australian summer monsoon and found little evidence to support the conclusion that a warmer climate would lead to an increase in precipitation during the northern Australian monsoon. There are however important caveats to note from this study, including that the models ranged from showing a 40% increase in precipitation, to a 40% decrease in precipitation during the summer monsoon (Brown et al. 2016). In the drier models, there appeared to be a significant warming of the equatorial western Pacific region, which enhanced rainfall over the western Pacific and away from northern Australia (Brown et al. 2016). The wetter models suggested increases in temperature over the central and eastern equatorial Pacific oceans, with a corresponding increase in precipitation over northern Australia (Brown et al. 2016). These results suggest that in order to accurately model

and project rainfall over northern Australia, model SST biases in the equatorial Pacific region need to be reduced, such that the true climatic influences over northern Australia can be seen (Brown et al, 2016). Seeing as the CMIP6 models are an improvement over the CMIP5 models, perhaps there is an opportunity to make more conclusive determinations about the magnitude and the direction of change of the northern Australian monsoon precipitation.

Despite the lack of conclusive results from more recent studies, it is worth noting that some studies have suggested an increase in precipitation over northern Australia as a result of anthropogenic forcing. One study using 20 climate models from CMIP5 found that there was an increase in precipitation of about 4.5% per degree Celsius of warming in the Asian-Australian monsoon (Wang et al, 2014). Most of this precipitation increase was attributable to an increase of about 5% per degree Celsius over the Indian subcontinent, but there was a noted increase over the northern Australian domain as well (Wang et al, 2014). The study of these 20 coupled models showed an increase in precipitation over northern Australia of about 2.3% per degree Celsius of warming (Wang et al, 2014).

Overall model data has been largely inconclusive on the potential trends in precipitation during the northern Australian monsoon season. However there have also been studies analyzing observational trends. Several studies have indicated an increase in precipitation over northern Australia during the monsoon season. Most recently Uehling and Misra (2020) observed a strong linear upward trend in precipitation in the 20th century over the region (Figure 1).

It is also worth noting that the study found increasing trends in the length of the monsoon season as well. The time series of the length (Fig. 1a), corresponding Onset date (Fig. 1b), and retreat date (Fig. 1c) of the NARS clearly indicate strong linear trends whose slopes pass the Mann–Kendall statistical significance test at a 99% confidence interval

(Hirsch and Slack 1984, Uehling and Misra, 2020). This figure was generated using the area averaged (aggregate) rainfall data over the northern Australian domain for each day. Figure 1 suggests that length of the season is increasing at the rate of 0.34 days per year (Fig. 1a), the onset date of the NARS is occurring earlier at the rate of 0.18 days per year (Fig. 1b), and the demise date is occurring later at the rate of 0.15 days per year (Fig. 1c). These changes in the length of the NARS have led to a corresponding increase in the amount of seasonal accumulated rainfall, which is seen to be increasing at a rate of 2.85 mm per year (Fig. 1d) (Uehling and Misra, 2020).

The time series of the seasonal rain, in units of daily rain rate in Fig. 1e shows a similar increasing trend of 0.01mm per day, per year. Fig. 1e clearly suggests that the NARS has an increasing trend of the seasonal accumulation of rain not only from an increasing length of season, but also due to an increasing mean daily rain rate (Uehling and Misra, 2020).

These trends lead to some interesting questions regarding the future climate of the NARS. It is worth investigating further to determine whether these observational trends are reflected in the models and if these trends will continue to persist in a warming climate. Ultimately, the question of whether anthropogenic climate forcing will have a significant impact on the northern Australian region is a question that remains unclear and thus going forward this question will be further investigated.

CHAPTER 2

OBJECTIVES AND METHODOLOGY

In our previous study, Uehling and Misra (2020) diagnosed the onset and retreat of the NARS based on the aggregate rainfall over the entire northern Australian monsoon domain (Figure 2).

Uehling and Misra (2020) defined the onset and the retreat dates of the NARS as the first and the last days of the year when the daily rain rate averaged over the entire domain of northern Australia (Figure 2) exceeded or fell below the climatological annual mean rain rate, respectively. As an obvious extension to this work, the following four specific objectives are proposed as part of this project.

2.1 Specific objective 1: Diagnosis of local onset/demise of the northern Australian rainy season:

The onset and the demise of the aggregate NARS was diagnosed following Liebmann et al. (2007) and Noska and Misra (2016). This methodology allows for a very clear and robust definition of the rainy season, and it has the additional advantage of only relying on widely available rainfall data (Uehling and Misra, 2020). In the study, the daily rainfall was averaged over the northern Australian domain outlined in Figure 2. This allowed for an area averaged cumulative anomaly curve of daily rainfall to be computed for each individual year.

2.1.1 The Observed Rainfall Analysis Dataset

The data used in this study for calculating both the local rainy season as well as to perform the MSSA analysis was sourced from the Australian Bureau of Meteorology's rain gauge network across the Australian continent (http://www.bom.gov.au/climate/how/newproducts/IDCdrgrids.shtml; Grant 2012). The dataset is available on a 0.5° grid over the Australian landmass. The data ranges from January 1, 1900 through until December 31, 2015 for a total time period of 115 years of data (Uehling and Misra, 2020). Though there are notable areas of sparse data, namely in the Australian outback, these data issues are less of an obstacle for this study, as the region of focus is very well covered with rain gauges throughout the time period. This complete dataset going back to over 100 years provides an extensive record to perform robust analysis of the data.

The rain gauge network does not align perfectly with the 0.5° grid that the dataset utilizes, which necessitates an algorithm to transpose the rain gauge data onto the grid. Using an optimized Barnes successive correction technique, the rain gauge data was transposed onto the 0.5° grid (Jones et al., 2009). This methodology applies a weighting average to each of the stations over Australia which can then be extrapolated to fit the grid (Grant, 2012). The daily rainfall values have a root mean square error of 3.1 mm and a mean absolute error of 0.9 mm (Grant, 2012). The dataset is also decomposed into a long-term average component and also an anomaly component (Grant, 2012).

Some noteworthy limitations of the dataset itself are mentioned by Grant, 2012. The data grid itself could not be any more precise due to the sparseness of gauges (in particular in the outback and other more rural areas), which does limit the accuracy of the data somewhat, however as previously mentioned, the absolute error is still small. In regions with a high observational density, or where there are strong gradients, the data-smoothing technique applied

to the data could potentially result in certain grid-point values that differ from the rainfall amounts at the contributing stations (Grant 2012). These issues are limited in this study due to the region of study. The northern Australian region has had a relatively dense observational network throughout the time period covered in this dataset.

2.1.2 Defining the Local Onset and Demise

The cumulative anomaly curve of the daily area averaged precipitation was computed using the formula (Uehling and Misra, 2020):

$$A_m(i) = \sum_{n=1}^{i} \left(\bar{r}_m(n) - \bar{\bar{r}}\right) - - - - - - - - - - - - - - - - (1)$$

where, $A_m(i)$ is the cumulative anomaly curve of the area averaged precipitation for day i of year m, $\bar{r}_m(n)$ is spatially averaged rainfall over northern Australia for day *n* of year *m* and $\bar{\bar{r}}$ is the area average, annual mean climatology of rainfall following , Uehling and Misra, (2020):

$$\bar{\bar{r}} = \frac{1}{MNK} \sum_{m=1}^{M} \sum_{n=1}^{N} \sum_{i=1}^{K} r(m,n,i) - - - - - - - - - - - - - - (2)$$

where, the summation over *i* is for area average by averaging over all K grid points over northern Australia, summation over *n* is averaging over all N days of the year for getting the annual mean and the summation over *m* is over all M years (1901-2015) to obtain the climatology of the annual mean. It may be noted that in the summation, $n = 1$ and N in Equation 1 is July 1 of a given year and June 30th of the following year, respectively. The minima and maxima in the $A_m(i)$ curve correspond to onset and demise date of the rainy season, respectively.

The analysis for the local onset/demise diverges from the analysis performed in Uehling and Misra (2020), when we no longer use the area averaged rainfall values but use the discrete rainfall data at every grid point of the rainfall analysis independently. It should be noted that the

spatial variability of the data is lost when area average is performed. For this reason, a methodology like that employed in Misra et al. (2017) is adopted for this study to resolve the potential spatial heterogeneity in the features of the rainy season. Misra et al. (2017) define local onset/demise of the Indian monsoon at every discrete grid point of the rainfall analysis over India using a similar methodology as elaborated in Equations (1) and (2) but applied at every grid point. However, to avoid the likelihood of detecting false onset/demise dates on account of synoptic or mesoscale variability that may be unrelated to the monsoon evolution, Misra et al. (2017) hinged the diagnosis of the local onset and demise dates to the climatological local onset and demise dates in the following manner:

In order to calculate the local onset, we compute the climatological daily cumulative anomaly of the local daily rainfall climatology ($lc_x(i)$) using the following formula:

$$lc_x(i) = \sum_{n=1}^{i} [\bar{r}_x(n) - \bar{\bar{c}}_x] \text{ - - - - - - - - - - - - - (3)}$$

where, $\bar{r}_x$ is the climatological daily rain at grid point x for day n, and $\bar{\bar{c}}_x$ is annual mean climatology of rain at grid point x (Misra et al. 2017). $\bar{\bar{c}}_x$ was computed using the following formula:

$$\bar{\bar{c}}_x = \frac{1}{days * years} \sum_{m=1}^{days} \sum_{n=1}^{years} r(m,n)_x \text{ - - - - - - - - - - - - - - (4)}$$

Where *days* are the number of days in a year, and *years* are the number of years in total (in this case 114, for the entire length of the Australian observed rainfall dataset). Figure 3 shows an example of how the cumulative anomaly curve can be calculated for a given grid point (for instance over Darwin, Australia). The local onset and demise can be computed as the minimum and the maximum of the cumulative anomaly curve at each of the grid points, respectively for each year.

Figure 3 demonstrates the cumulative anomaly curve methodology for the climatological data for Darwin, Australia.

Once the local onset and demise is computed at each grid point for all years, the data can be averaged over all years to arrive at a climatological value at each grid point. The climatological values for onset, demise, and length of the rainy season are shown in Figure 4a, b, and c, respectively. Additionally, using climatological rainfall values for each day, a climatological seasonal rainfall value can be calculated for each grid point (Figure 4). We then compute the difference (b_x) between the climatological local ($\overline{o(lc}_x$) and climatological overall Australian (area averaged over northern Australian) rainy season onset ($\overline{O(i)}$) as:

$$b_x = \overline{o(lc)_x} - \overline{O(i)} \quad (5)$$

and similarly, the difference (d_x) between the climatological local ($\overline{d(lc}_x$) and area averaged over northern Australia demise ($\overline{D(i)}$) as:

$$d_x = \overline{d(j)_x} - \overline{D(i)} \quad (6)$$

The climatological departures of local with area averaged onset/demise over the 114-year period of the dataset gives a robust estimate of the phase lag (in days), with the transients being averaged out. We then define local onset ($lc_m(i)_x$) and demise ($ld_m(i)_x$) for a given year *m* and grid point *x* from the daily cumulative anomaly for the year *m* by finding conservatively (the nearest) minimum and maximum near the immediate vicinity of ($O_m(i) \pm kb_x$) and ($D_m(i) \pm pd_x$), where, $k = \left(1 + q\sigma_{b_x}\right)$ and $p = \left(1 + r\sigma_{b_x}\right)$, $\sigma_{b_x}, \sigma_{d_x}$, are the standard deviations of b_x and d_x, q and r are fractions that are incrementally increased from zero.

2.2 Specific objective 2: Understanding the influence of the intraseasonal variations on the evolution of the northern Australian rainy season

In order to gain more insight into the intraseasonal oscillations of the NARS, a multichannel singular spectrum analysis (MSSA) was performed. MSSA has been used in many fields of study over recent decades and its usefulness allows it to be applied to many different areas of study, including in this case to the NARS (Ghil et al. 2002; Karmakar et al. 2017). The advantage to using the MSSA technique rather than a simpler harmonic analysis or Fourier transform is that the shape and bandwidth of the MSSA filters are themselves functions of the input data (Karmakar et al. 2017). Singular spectral analysis is utilized to extract information from short and noisy time series (in this case from rainfall data, which is an inherently noisy data series; Allen-Robertson, 1996; Moron, 1998; Ghil et al. 2002). Ghil et al. (2002), lays out the details for the computation of the MSSA. MSSA allows for a systematic extraction of the individual spatio-temporal modes and allows for the intraseasonal oscillations to be very easily extracted and identified (Karmakar et al. 2017).

In order to determine the phases of the intraseasonal oscillations, equation 7 was utilized.

$$\gamma(t) = Arg(Y'(t) + iY(t)) \quad (7)$$

In equation 7, t denotes time, Y(t) is the n-day long intraseasonal oscillation time series over a specified grid point. (′) indicates the time-derivative calculated using central differences. Arg(z) represents the principal value of the phase of a complex number z=x + iy. γ(t) is calculated for each year separately and lies between −π and π (Karmakar and Misra, 2019). The entire phase plane for ISO at any location can be divided into 8 equally spaced intervals such that $-\pi + (m-1)(\pi/4) \leq \gamma(t) < -\pi + m(\pi/4)$, m = 1, . . . , 8 (Karmakar and Misra, 2019). Phases 1 to 4 corresponds to the negative part of ISO, while phases 5 to 8 are linked with the positive values of

ISO. Using these values of the phase angle, each grid point can be assigned a state of the ISO in terms of a phase, which can be further used to create phase composite diagrams.

The MSSA methodology uses the convolved space time PC's (ST-PCs) of the EOF's and the reconstructed components (RCs). The phase components cannot be orthogonal because they are describing the phase angle of a particular band of frequencies. The different phases indicate the phases of the MJO that are divided in 8 equal phases from -pi to pi or 0 to 2pi (Karmakar and Misra, 2019).

The MJO is the primary intraseasonal oscillation over the northern Australian domain (Wheeler et al. 2004, Wheeler et al. 2012, Zhang et al. 2013). Specifically, over northern Australia, the precipitation anomalies associated with MJO are noted (Zhang et al. 2013). The MJO operates over a timescale of 30-90 days, which matches the window over which our MSSA analysis is performed. Due to the well observed influences of the MJO on precipitation over the northern Australian domain during the austral summer months, the diagnosed oscillations seen in the MSSA analysis can be safely attributed to the MJO. There are no other known possible ISOs that operate on the same timescale over the northern Australian domain.

Using the MSSA technique, the phase composites were computed for each year from 1900 to 2015. Only the rainfall data from the time surrounding and including the NARS was used, rather than for the entire year. This ensures that the signals being seen were signals that were originating from ISOs during the monsoon season, not from other times of the year. To capture all ISOs for all years, the analysis was performed from Julian day 290 (October 17th) to Julian day 120 (April 30th) of the following year. This wide range of dates ensures that every rainy season is fully analyzed with sufficient days surrounding the rainy season to ensure that the MSSA technique works accurately. Additionally, eight phase composites were chosen, as eight phases are a

common choice to use when analyzing ISOs or oscillatory modes in the atmosphere (Ghil et al 2002, Karmakar et al. 2017, Karmakar and Misra, 2019).

As an example, the following phase composite diagrams were produced using data from the 2014-2015 monsoon season (Figure 5). Phases 1-4 are the wet spell and phases 5-8 are the dry spell of the ISO. The peak phase of the wet spell is phase 3 and that of the dry spell is phase 7. Each of these phases are approximately 6-7days long, with the wet and dry spells lasting ~20 days each.

Once the phase composites were calculated for each monsoon season, the phase composites could be computed as an average for all years. The 8 phases are calculated based on rainfall over northern Australia as described previously.

In addition, a randomization test is performed in some places to determine the significance of the results. The null hypothesis in this case is that the values observed are coming from a distribution with a zero mean. Then we generated 1000 bootstrap samples using the observed samples. If zero is outside the middle 95% of sorted bootstrap samples, then we reject the null hypothesis at 5% significance level.

2.3 Specific objective 3: Diagnosing the fidelity of the northern Australian rainy season in the CMIP6 historical simulations

The release of the new CMIP6 models provides an opportunity to gain further insight into the potential changes in the monsoon due to anthropogenic forcing. The new CMIP6 models have already been shown to be an improvement over the predecessor CMIP5 model generation (Narsey et al 2020; Brown et al. 2016). The new CMIP6 models show a reduced equatorial Pacific cold

tongue bias when compared to the older CMIP5 models (Narsey et al . 2020). It was also noted that the new CMIP6 models show improved northern Australian rainfall teleconnections with large-scale climate drivers and improved representation of atmosphere and ocean extreme heat events (Narsey et al. 2020). These improvements over the older generations of the CMIP models allow for better conclusions to be made with regards to the Australian monsoon.

In order to diagnose the fidelity of the CMIP6 models with regards to the NARS, the previously defined definition for the length of the NARS (Uehling and Misra, 2020) will be applied to the model output using the area average aggregate over northern Australia versus the previously utilized local definition. The model outputs can be analyzed to determine whether they resemble the observed seasonal evolution of the rainy season and its variations. The fidelity of the historical 20th century simulations of the CMIP models is often used as a metric to assess the reliability of the future projections of climate (Shukla et al. 2006). Once this baseline analysis has been performed, it can be determined which models are best for use over the northern Australian region. Ideally there will be several models which perform well enough to be used to diagnose future climates over northern Australia.

2.4 Specific objective 4: Understand the projections of the northern Australian rainy season in a future warming climate.

Using the most representative models, the future climatology of the northern Australian monsoon can be better understood. Ideally questions about the magnitude and direction of potential changes to the monsoon can be quantified more definitively. Prior investigations into this question have been inconclusive (Narsay et al. 2020, Brown et al. 2016). It is important not

just to note how precipitation trends are changing, but also whether the season is getting longer/shorter or if the timing of the season (or the seasonal cycle) is changing.

As the primary precipitation driver for northern Australia, having a more complete understanding of the impacts of climate change on the monsoon are vitally important. Observational trends over northern Australia have shown upward linear trends in both the length of the NARS, as well as in the amount of rainfall during the season (Uehling and Misra, 2020). It is vitally important due to the socio-economic and climatic concerns in the region to understand what could be causing these observed trends and whether they will continue. Climate change is one of the most important issues to be faced in the coming decades, and due to the current unknowns surrounding the questions of potential anthropogenic forcing on the northern Australian monsoon it will be important to investigate these questions.

The objective definition of the onset and the retreat of NARS follows from Uehling and Misra (2020). Here, it should be noted that the daily rainfall anomalies are computed relative to the annual mean climatological rainfall. The chances of the diagnosis of false onset or retreat dates of NARS from random thunderstorms are unlikely because the rainfall is area averaged over a relatively large domain. Once these dates of onset and retreat of NARS are diagnosed for each year then the seasonal rainfall is computed as accumulation of the daily rain rate between these dates, which unlike the traditional fixed length season accounts for both variations in daily rain rate and length of the season. This procedure is repeated on all 24 CMIP6 models over all three simulations.

To compute the trends for each of the models, the non-parametric method following Sen's slope methodology (Sen 1968) using the R package 'wq' (Jassby and Cloern 2015) was used. The Mann-Kendall test with Sen's slope estimator is used to detect the significance of the

trend (e.g., Xu et al. 2003, Partal and Kahya 2006). This methodology is advantageous as it reduces the influence of outliers to produce a more representative value for the true trend of the data (Sen 1968, ElNesr et al. 2010, and Meals et al. 2011). Additionally standard t-tests are applied to the correlations which were calculated to determine the significance of the correlation.

CHAPTER 3

BACKGROUND

3.1 Rainy season vs Monsoon season

Most of the prior studies have focused on the Australian summer monsoon season. Several studies like Nicholls et al. (1982) and Nicholls (1984) recognized however, that the rainy season starts earlier and lasts longer than the typical northern Australian monsoon season (Nicholls et al. 1982; Nicholls 1984; Uehling and Misra, 2020). The northern Australian monsoon, also known as part of the Asian-Australian monsoon, occurs between the months of November and March, and this phenomenon results in enhanced precipitation over the northern Australian region (Troup 1961; McBride 1983, 1986; Nicholls 1984; Wang 2003). The monsoon rains are the result of west to northwesterly winds bringing enhanced tropical moisture over northern Australia (Troup 1961). This moisture originates in the tropical western Pacific Ocean and the Indian Ocean, and the west/northwesterly winds drag this moisture south over the Australian continent (Troup 1961; Murakami and Sumi 1982). Due to the aridity of much of Australia, the rainy season over northern Australia is incredibly important and has wide socio-economic and environmental implications (Anwar et al. 2007; Qureshi et al. 2013).

There is a difference between the NARS and the monsoon season, which was first noted by Nicholls et al. (1982) and Nicholls (1984). These studies observed that the rainy season typically starts earlier and lasts longer than the northern Australian monsoon. There however, remains significant overlap between the monsoon season and the rainy season. The typical peak

of annual rainfall in the rainy season of northern Australia coincides with the seasonal peak of its monsoon season (Atkinson 1971; Davidson et al. 1983, 1984; Holland et al. 1986).

There have been many different studies describing the seasonality of the northern Australian monsoon. These studies have utilized different definitions for the monsoon, and they analyzed varied datasets. Many studies used a wind-derived definition of the monsoon, such as defining the onset and the demise of the northern Australian monsoon as the first and the last days of westerlies at 850 hPa over Darwin (Holland 1986). Other studies instead choose to use rainfall data to derive their definitions (Smith et al. 2008, Lisonbee et al. 2020, Uehling and Misra 2020). There are many advantages to using a rainfall-based definition, including the easy accessibility of data, the completeness of the data, the time length of the record, and the simplicity of the definition (Uehling and Misra 2020).

3.2 The Northern Australian Rainy Season Domain

The primary region where the monsoons effects are the strongest in northern Australia which encapsulate a region between 10° S - 20°S, and 120° E - 150°E (Figure 2), where the annual peak of the rainfall coincides with the monsoon season (Atkinson 1971; Davidson et al. 1983, 1984; Holland et al. 1986; Uehling and Misra, 2020). Figure 2 shows the primary region of focus. Extending the domain any further south would include the central part of the Australia continent, which is characterized by an arid climate and is a region in which the monsoon effects are not felt.

3.3 The rainy season index

The index outlined in Uehling and Misra (2020) provides numerous advantages over other methodologies to describe the NARS. First, this index relies only on one variable, rainfall. Rainfall data, as mentioned earlier, is reliable and the record is quite complete over the region dating back more than 100 years. This ensures that the season lengths computed using this methodology are reliable and robust over an extensive period of time. Additionally, other atmospheric variables, such as upper air observations are less reliable, less spatially extensive over the region, and also the length of the records aren't as long (Uehling and Misra, 2020).

The onset and the demise of the wet season is recognized to be spatially non-uniform process (Tanaka 1994; Murakami and Matsumotno 1994; Misra et al. 2017; Uehling and Misra, 2020). This is the reason for expanding on the previous work of Uehling and Misra (2020). In that paper, an area averaged rainfall analysis was performed. The index that they used was based on the area averaged rainfall across the northern Australian domain (Figure 2). These large-scale indices are relatively less sensitive to the temporal variations of the density of observations and are therefore useful in robustly diagnosing the existence of any climate change signal. However, there are significant and noteworthy spatially non-uniform features of the rainy season that are not apparent when using area averaged data. For this reason, the local onset and demise calculations were performed so that the spatial differences in the NARS would become apparent.

3.4 The intraseasonal oscillation and the evolution of the rainy season

Currently there exists only limited research on the intraseasonal oscillations of the northern Australian monsoon season. One such study looked specifically at the Community Earth System

Model Version 2 (CESM2) to analyze various global monsoon features and their intraseasonal oscillations (Meehl et al. 2020). Their analysis of the Asian-Australian monsoon noted major flaws with the model, including that there is about 20% less precipitation shown over northern Australia in the models compared to observations (Meehl et al. 2020). This could potentially be due to the overly strong cold tongue in the Pacific, leading to suppressed convection over the maritime continent (Meehl et al. 2020). The authors do note that the CESM2 model does a much better job of portraying the dynamical features of the monsoon, including improvements in both the low-level winds and the well defined monsoonal flow (Meehl et al. 2020).

The onset and the retreat of the Northern Australian wet season are also associated with the intra-seasonal variability (Troup 1961; Hendon et al. 1989; Hendon and Liebmann 1990a, b; Krishnamurti et al. 1995; Wheeler and Hendon 2004). With regards to the intraseasonal oscillations that are important to the northern Australian monsoon, the Madden-Julian Oscillation (MJO) appears to be of primary importance (Pope et al. 2009, Wheeler and McBride 2012, Meehl et al. 2020). The MJO has a very consistent propagating signature in the Indo-Pacific region which shows the eastward propagation through the northern Australian region. Figure 6 reflects the differences in the MJO signature as seen in the CESM2 model when compared to the CESM1 model (Meehl et al. 2020). The CESM2 model is a much improved upon version of the CESM1 as it has upgraded the representation of many physical processes that affect monsoon dynamics (Meehl et al. 2020). Features that were improved upon include boundary layer dynamics, shallow convection processes, convective schemes, and precipitation processes (Meehl et al. 2020). Figure 6a, b, and c reflects the zonal propagation of the MJO through the equatorial Pacific region between 60°E and 90°E for the observational data, CESM2, and CESM1, respectively. In the observations and the CESM2 data, it can be seen that the MJO propagation is much clearer and extends through

the Australian monsoon region (Meehl et al. 2020). In Figure 6c, the ISO is contained within the Indian Ocean and does not show the propagation that is observed, as seen in panel a (Meehl et al. 2020). The second row of panels in Figure 6 (d, e, and f) display the same but for the meridional propagation of these features between 10°N and 20°S. It is similarly shown that in the CESM2 data there is a more clear and coherent southward propagation of anomalies (Figure 6e), which more closely matches observations (Figure 6d). It is apparent that CESM2 performs significantly better at replicating the propagating features of the intraseasonal oscillation in the region when compared to CESM1, and this is due to the aforementioned improvents in the way the model handles dynamical processes that directly impact monsoons.

The MJO is one of the most important drivers of intraseasonal features of the NARS, however recent studies have also noted midlatitude influences as well. Rainfall "bursts" during the NARS are often accompanied by a notable increase in cyclonic circulation with the monsoonal region (Narsay et al. 2017). Front-like mid-latitudinal features can drive dynamical changes in the monsoon region leading to bursts of heavier precipitation rates throughout a monsoon season (Narsay et al. 2017). It was found that the most important influence on monsoon burst circulation changes is the absolute vorticity fluxes and that all other influences (including the MJO) accounted for only one-third of the burst events (Narsay et al. 2017).

With most studies focusing on the influence of the MJO as the primary driver of the intraseasonal oscillations, it is clear that the MJO is worth investigating to determine not only its role in the intraseasonal oscillations of the monsoon, but also what role (if any) it plays on the onset and the demise of the rainy season.

3.5 Climate change and the rainy season

Climate change is a topic that has received much attention in both the scientific community and the public at large. The implications of anthropogenic climate change, and its potential impacts have great environmental and socio-economic concerns. Recently, the CMIP6 model runs have been completed, which provides an opportunity to assess the future climates under varying anthropogenic forcing.

The Coupled Model Intercomparison project is one of the major foundations of climate research (Eyring et al. 2016). The new CMIP6 models consist of three major elements, which are common experiments conducted by all the models, common standards used across the various simulations, and also an ensemble of CMIP endorsed Model Intercomparison Projects that are phase specific (in this case phase 6, or CMIP6) (Eyring et al. 2016). The common experiments performed by the models include the Diagnostic, Evaluation and Characterization of Klima (DECK) and also historical simulations from 1850 to the present (Eyring et al. 2016).

The Scenario Model Intercomparison Project (ScenarioMIP) for CMIP6 provides the multi-model climate projections, with varying scenarios that are based on future anthropogenic emissions and changes in land usage and are projections from 2015 to 2100 (O'Neill et al. 2016). The CMIP6 models utilize shared socioeconomic pathways (SSPs), which consider various emissions and land use scenarios to project future climates (O'Neill et al. 2016). SSPs 1 and 5 are the more optimistic future scenarios, with considerations for substantial investments in education and health, rapid economic growth, and well-functioning institutions (O'Neill et al. 2016). The major difference between SSP5 and SSP1 though is that SSP5 assumes an energy intensive, fossil fuel-based economy, whereas in SSP1 there is much more use of more sustainable fuels and energy sources, such as wind and solar technology (O'Neill et al. 2016). SSPs 3 and 4 are the more

pessimistic future scenarios where investments in education and healthcare are minimal, there are rapid population increases, and inequality continues to grow (O'Neill et al. 2016). These SSPs are more robust than the RCP scenarios that were the basis of future projections in the CMIP5 models due to the fact that the new scenarios have given more considerations about the socioeconomic aspects of these projections, hence the name shared socioeconomic pathways.

It is important to note the potential limitations of the CMIP6 models, particularly over the northern Australian region. There have been several previous studies that have analyzed the skill of the CMIP6 models themselves at simulating regional events (Brown et al. 2016, Narsey et al. 2020, Ridder et al 2020). These studies have found that the skill of the CMIP6 models vary greatly depending on the region of study. Over northern Australia, when compared to the observational record, the CMIP6 models appear to be somewhat less skilled (Narsey et al. 2020, Ridder et al. 2020). It is therefore worth noting these potential shortcomings when discussing the results of the CMIP6 analysis over northern Australia.

CHAPTER 4

RESULTS

4.1 Climatological local onset/demise of the northern Australian rainy season

The onset/demise dates of the NARS was computed for 114 years at every grid point of the domain shown in Figure 2. The red curve in Figure 3 shows the climatological cumulative rainfall anomaly curve over Darwin (12.4°S and 130.8°E), with the minima of the curve being the onset date and the maxima being the demise date of the rainy season. Climatologically, the onset date of the rainy season over Darwin occurs on Julian day 329 (~November 25th). Whereas the climatological demise date over Darwin is around Julian day 98 (~April 8th of the following year). It can also be seen that the definition used for calculating the local rainy season over Darwin corresponds to the time period of highest rainfall during the year (Figure 3).

Figures 4a and b show the spatial distribution of the local climatological onset and demise of NARS, respectively. It is noteworthy that NARS varies markedly across the domain. Figure 4a shows that the onset of NARS begins in the western portion of northern Australia earlier than in the eastern portion (Figure 4a). The earliest onset dates, on average, occur in the Northern Territories of northern Australia in a band around 130°E longitude. The onset generally occurs in this band around the 315-325th Julian day of the year. The land areas to the west of the Gulf of Carpentaria generally have earlier onsets than land areas to the east and south of the Gulf of Carpentaria (Figure 4a). In the eastern part of northern Australia, the average onset date of the rainy season ranges between 330-350th days of the year (Figure 4a).

Similarly, Figure 4b shows the spatial distribution of the climatological local demise dates of the NARS. The spatial distribution of the climatological demise date of the rainy season reflects the "lifting out" of the monsoon trough over northern Australia. As the monsoon season draws to a close, the contrast between the ocean and land temperatures reduces, which in turn leads to the monsoon trough lifting to the north away from the Australian continent. This is reflected in the observational data, which shows the earliest demise dates on average occurring to the south and the latest demise dates occurring in the northernmost regions of northern Australia (Figure 4b). It may be noted that the monsoon trough generally appears to lift out of the region from southwest to northeast, as the demise dates follow a trend of later dates moving from southwest to northeast.

Figures 4c and d show the climatological seasonal length of NARS for each grid point, as well as the climatological seasonal rainfall that accounts for the spatially varying length of the season, respectively. The length of the rainy season generally increases from south to north. This makes logical sense, as the monsoon trough begins each season by moving south over the region and then lifting back out once again at the end of the season. It may be noted that the region of northern Australia that experiences the longest climatological rainy seasons is the region just to the west of the Gulf of Carpentaria that exhibited the earliest and the latest climatological onset and demise dates, respectively (Figure 4c). This region has rainy seasons that last on average longer than 140 days. Most of the rest of northern Australia experiences rainy seasons that last on average around 115-130 days (Figure 4c). Figure 4d shows the northernmost regions of Australia receiving the most monsoon-associated rainfall, with a general progression of less rainfall as one moves further south towards the Australian interior. Near the northern and eastern coasts of northern Australia, climatological rainy season rainfall averages to over 500 mm per year. These

values decrease as one moves south to the southern reaches of the domain with the climatological seasonal rain reaching around 100-200 mm per year.

Figures 7 and 8 show the progression of the climatological local onset and local demise with respect to the aggregated NARS onset and demise, respectively. In Figure 7, we see that the earliest climatological local onsets occur nearly 10 days before the climatological onset of the aggregate NARS in the northern tip of the Northern Territory and the northeastern tip of the Western Territory of Australia. Then the climatological local onset slowly progresses eastward and southward before a majority of northern Australia achieves its climatological local onset by around 8 days after the aggregate NARS climatological onset (Figure 7). Furthermore, by day 19, after the climatological onset of the aggregate NARS onset, the remaining portion of the horn of Australia also achieves its climatological local onset (Figure 7). Similarly, the climatological local demise date appears first along the southern tip of the northern Australian domain almost 10 days before the climatological demise date of the aggregate NARS is reached (Figure 8). The climatological local demise date then slowly progresses northward before all of the domain achieves the climatological demise by the 19th day after the climatological demise of the aggregate NARS is reached.

The composite daily rain rates from 10 days prior and 9 days post local onset of the rainy season are shown in Figure 9. Figure 9 shows that the climatological daily rainfall values prior to the day of local onset are lower than the values after the local onset of the rainy season. Furthermore, the strong north-south gradient of rainfall over northern Australia is maintained throughout this evolution, with the northern coastline region receiving the most rainfall while the southern interior of the domain receives relatively less rainfall. Similar features are also observed

around the demise date, with the exception that rain rates decline in the post local demise period relative to days prior to the local demise date (Figure 10).

4.2 Interannual variability of the rainy season

There is a strong relationship between the variations of the local onset date and the local seasonal length of NARS (Figure 11a). The negative correlations between the onset date and the seasonal length in Figure 11a suggest that earlier or later onset date at a given grid point is associated with longer or shorter rainy season, respectively. Figure 11a shows the strongest negative correlations are in the northern part of Australia, which is also the region with the earliest onset dates in the domain (Figure 4a). Similarly, Figure 11b shows the correlation between the local onset date and the corresponding seasonal rainfall anomaly. This figure demonstrates that there is a generally strong negative correlation between the onset date and the seasonal rainfall anomaly, suggesting that early or later onset is associated with wetter or drier rainy season, respectively. Therefore, Figures 11a and b strongly suggest that monitoring the variability of the local onset date of the rainy season over northern Australia can serve as a good seasonal outlook for the following rainy season in terms of its seasonal length and seasonal rainfall anomaly.

Figures 12a and b show the correlations of the variations of the retreat date with the seasonal length and seasonal rainfall anomalies of NARS, respectively. The correlations in Figures 12a and b are positive, suggesting that early or later retreat of the rainy season is associated with shorter and drier or longer and wetter rainy season, respectively. Figures 12a and b also suggest that monitoring the retreat date variations of NARS could be useful to posteriorly analyze the

season. Interestingly, the correlations between the local onset and the corresponding local retreat date variations are statistically insignificant (not shown).

The ENSO teleconnection with NARS is significant (Holland 1986; UM20). UM20 showed that this teleconnection becomes stronger when the variations of the length of the aggregated NARS is considered. Figure 13a shows that there is a strong positive correlation between the September-October-November (SON) seasonal mean Niño3.4 (ENSO) SST anomalies and the local onset date suggesting that warm or cold ENSO SST anomalies are associated with later or early local onset of NARS, respectively. This relationship tends to be strongest east of the Gulf of Carpentaria (east of 140°E; Figure 13a). The opposite relationship is shown between the SON seasonal mean ENSO SST anomalies and the local retreat date of NARS (Figure 13b). The correlations between Niño3.4 SST anomalies and the corresponding retreat date variations are, however, weaker (Figure 13b) relative to variations with the onset date variations (Figure 13a). This relationship also manifests in and is reflected by the negative correlation between the SON seasonal mean ENSO SST anomalies and the local seasonal length variations (Figure 13c). The correlation in Figure 6c implies that warm or cold SON seasonal mean ENSO SST anomalies are associated with shorter or longer seasonal length of the rainy season over northern Australia, respectively. Again, the variability between the ENSO SST anomalies and seasonal length are comparatively stronger to the east of Gulf of Carpentaria (Figure 13c). Finally, the correlations between the SON Niño3.4 SST anomalies and seasonal rainfall anomaly (Figure 13d) nearly mimic the correlations with seasonal length (Figure 13c), suggesting that warm or cold ENSO anomalies are associated with the drier or wetter season. In comparison, the correlations of the SON ENSO SST anomalies with fixed length December-January-February seasonal rainfall anomalies over northern Australia are largely confined to east of 140°E (Figure 13e). The

comparison of Figs. 13d and e clearly illustrate the importance of accounting for the spatial heterogeneity of NARS. More importantly we conclude that acknowledging the variations of the local seasonal length of NARS in computing the seasonal rainfall anomaly is critical to diagnose the ENSO teleconnections over the region.

4.3 Intraseasonal variations of the rainy season

By utilizing the MSSA methodology described previously, rainfall phase composites of the ISO rainfall during November–May 1900–2015 was generated (Figure 14). These phase composites reveal that during the first 4 phases of the ISO, on average, there is enhanced precipitation over the northern Australian domain, suggesting a wet spell while the remaining 4 phases represent the dry spell (not shown). A spatial distribution of the frequency of the local onset and retreat dates of NARS in each of the eight phases of the ISO is shown in Figure 15. The largest density of local onset of NARS occurs around the Gulf of Carpentaria in Phases 4 and 5 of the ISO (Figure 15a). In the first four (wet) phases of the ISO, the frequency of local onset is lower (44.65%) than in the latter four (dry) phases of the ISO. This feature is also illustrated by the relative frequency (=number of onset in each phase that is statistically significant/total number of local onsets in all phases in statistically significant regions) in Figure 15b. Figure 15b indicates that most local onset occurs in the wet spell phases of 1 and 4 of the ISO and in phases 5 and 8 of the dry spell of the ISO. We observe from the spatial distribution of local onsets in Figure 15a that there is no coherent pattern of local onset occurring in the wet and dry spells of the ISO to suggest that one region of the domain is more conducive than the other for local onsets to occur in the wet/dry phases of the ISO.

Similarly, the spatial distribution of the frequency of the local retreat date within the different phases of the ISO is shown in Figure 16a. We observe that some of the highest density of local retreat occurs in phases 7 and 8 of the ISO, while in the remaining phases of the ISO the frequency of local retreat is more uniform across the domain (Figure 16b). In contrast to the frequency of local onset, the local demise of NARS occurs 71.31% in the dry spells (Phases 5 to 8) of the ISO. We find from Figure 16a that most of the local demise of NARS during dry spell of the ISO occurs around the Gulf of Carpentaria and in the southeast region of the domain. The southwest region of the domain uniquely exhibits a high density of local demise of NARS during Phase 3 (wet spell) of the ISO.

4.4 Climatology of the CMIP6 historical simulations

The climatological onset dates of NARS in the CMIP6 historical simulations display a wide range of values around the observed climatological onset date of 341 Julian day (~December 7th; Fig. 1a). A majority (i.e., 16) of the models show a later onset than observations. However, 21 of the 24 models have their climatological onset date of NARS within one standard deviation of the observed climatological onset date (Fig. 18a). Three models, namely, INM-CM4-8, INM-CM5-0, and MIROC-ES2L show a climatological onset date earlier than the corresponding observations by more than one standard deviation.

The observed climatological retreat date of NARS is Julian day 90 (~March 31; Fig. 18b). In relation to the onset date (Fig. 18a), the range of the climatological demise date across the CMIP6 historical simulations is relatively less (Fig. 18b) with earliest occurring on Julian day 79 (~March 31; MIROC-ES2L) and latest occurring on Julian day 105 (~April 15; NESM3). All the

models display their climatological retreat date of NARS within one standard deviation of the corresponding observations (Fig. 18b). As a result of the variations of the climatological onset and retreat dates of NARS across models, the climatological length of NARS in the CMIP6 historical simulations shows a rather large range from 96 days (MPI-ESM1-2-HR) to 152 days (INM-CM4-8) relative to the observed climatological length of 115 days (Fig. 18c).

The climatological seasonal rainfall for the fixed length NARS, which is December through March (DJFM) and that for varying length of NARS shows considerable differences (Fig. 19). For example, in Fig. 19a the observed DJFM climatological seasonal rainfall is 590mm while it is 419mm for a varying length of NARS in Fig. 19b. Similarly, the range of the climatological seasonal rainfall for the DJFM season displayed by the CMIP6 historical simulations in Fig. 19a from 343mm to 1228mm is slightly different from the range of 357mm to 1351mm for varying length NARS in Fig. 19b. Hereafter, we will be focusing on varying length NARS.

4.5 Bias in the historical simulations of CMIP6

The scatter between the climatological bias of the onset and retreat date of NARS indicates that 12, 4, 2, and 6 models display late onset bias with a late retreat bias, late onset bias with early retreat bias, early onset bias with early retreat bias, and early onset with late retreat bias, respectively (Fig. 20a). In other words, 14 of the 24 models display bias of the same sign for the onset and retreat of NARS, which suggests that the bias is stemming from the shift of the seasonal cycle of NARS besides varying the seasonal length in these models. In the rest of the models where the onset date and retreat bias have opposite signs it implies that the length of NARS is getting stretched or compressed relative to observations. Most of these models display a bias in the onset

and retreat dates of NARS in the range of 5 to 15 days with a few outliers showing over 30 days (Fig. 20a). In Fig. 20b, we find that 12 of the 24 models with late onset bias also display a bias of a shorter length of NARS while 8 models of the 24 show a bias of longer length of NARS with early onset bias. It may be noted that most of the models display a length of the season bias in the range of -15 to +15 days with some outliers greater than 30 days (Fig. 20b). Similarly, a majority (12 of the 24 models) show a positive bias in the seasonal rainfall of NARS that display a late onset bias (Fig. 20c). Only 4 models show a dry bias with late onset bias of NARS while 8 models show a wet bias with early onset bias of NARS (Fig. 20c). The wet bias in seasonal rainfall is significant with most of the models (21 of the 24) showing more than 100mm, with some outliers over 600mm (Fig. 20c). However, the relationship of the bias in seasonal rainfall of NARS with corresponding bias in the length of NARS is not that obvious (Fig. 20d). The bias in seasonal rainfall of NARS is contributed from both bias in the length of the season and bias in the daily rain rate. There are 12 models that display wet bias with a bias of longer length of NARS. However, there are 8 models with wet bias and 4 models with dry bias that display a bias of shorter length of the season.

4.6 Linear trends in the historical simulations of CMIP6

Uehling and Misra (2020) reported robust linear trends of earlier onset dates, later retreat dates, and increasing length of NARS with values of -0.18 days yr^{-1}, +0.15 days yr^{-1}, and +0.34 days yr^{-1}. In Fig. 21a, we find that the observed trend of the onset date of NARS is unmatched by any of the CMIP6 models. In fact, only one model (ACCESS-CM2) shows a statistically significant negative trend of the onset date with a value -0.07 days yr^{-1}. Similarly, the observed

positive trend of the retreat date is unmatched by any of the CMIP6 models with only INM-CM5-0 showing a statistically significant positive trend of +0.07 day yr^{-1}. In the case of the trends in the length of NARS, we observe yet again that none of the CMIP6 models can match the observed linear trend with only two models (NESM3 and NorESM2-MM) showing statistically significant positive trends. The historical simulations of CMIP6 similarly show an under representation of the positive linear trends in the seasonal rainfall of NARS (Fig. 21d). Even if the trend of the fixed length DJFM seasonal rainfall over northern Australia is computed, the CMIP6 models continue to underestimate the observed trends (Fig. 21e). This suggests that it is not only the secular trends in the length of NARS but also the lack of the linear trends in the daily rain rates of the CMIP6 models that are contributing to the bias displayed by the models. This overall underestimation of the linear trends in the parameters of NARS is a major limitation of the CMIP6 models that would have to be further investigated.

4.7 Interannual variations in the historical simulations of CMIP6

It was reported in Uehling and Misra (2020) that early or later onset of NARS is associated with longer or shorter length of the season and wetter or drier season, respectively. Similarly, early or later retreat date of NARS is associated with shorter or longer length of the rainy season and drier or wetter season, respectively. There is however no such linear relationship between the variations of the observed onset and retreat dates of NARS (Uehling and Misra 2020). In Table 2, we show the correlations between the various parameters of NARS from the historical simulations of CMIP6. In Table 2 the correlation between the onset date and demise date, the onset date and the seasonal rainfall anomaly, the demise date and the season length, the demise date and the

seasonal rainfall anomaly, and the seasonal length vs the seasonal rainfall anomaly is shown. The correlations between the onset date and demise dates are low as these are expected to be independent of one another. The onset date is negatively correlated with the seasonal length and the seasonal rainfall anomaly, which implies that earlier onsets lead to longer and wetter seasons. The demise dates are positively correlated with seasonal length and seasonal rainfall anomalies which implies that later onsets also lead to longer and wetter rainy seasons. A majority of the CMIP6 models show insignificant relationship between the onset and the retreat dates of NARS like the observations. In fact, the correlations of the onset date and the retreat date of NARS with seasonal length and seasonal rainfall anomaly and that of seasonal length with seasonal rainfall anomaly from the CMIP6 historical simulations in Table 2 verify remarkably well with observations.

ENSO variations have a significant influence on the interannual variations of these parameters of NARS (Uehling and Misra 2020). For example, a warm or cold ENSO event is associated with later or early onset date of NARS, respectively, which is displayed by most CMIP6 models (Fig. 22a). Similarly, warm or cold ENSO event is associated with early or later retreat date of NARS (Fig. 22b), albeit, with weaker correlation values than those with the onset date (Fig. 22a), which most CMIP6 models replicate. Furthermore, warm or cold ENSO events are associated with shorter or longer seasonal length of NARS (Fig. 22c) and drier or wetter seasonal anomaly (Fig. 22d), respectively. The historical simulations of CMIP6 models show reasonable fidelity in replicating these relationships in Figs. 22c and d. This is consistent with Grose et al. (2020), where they report that teleconnection of the Australian monsoon rainfall with ENSO has improved in CMIP6 relative to CMIP5 historical simulations. Grose et al. (2020) find that the CMIP6 models

have reduced the equatorial Pacific cold tongue bias west of the dateline, which may be one of the reasons for the improved teleconnection of NARS with ENSO in CMIP6.

4.8 The future climate projections under SSP585

SSP585 is the fossil fueled socio-economic pathway of the future, that raises the CO2 concentration non-linearly to about 1025 ppm from 2015 through 2100. The climatological difference in the onset date of NARS from this future projection with the corresponding historical simulation is shown in Fig. 23a. In this figure we find only 4 models that indicate a statistically significant difference with three models showing an earlier onset in the future climate. Similarly, the change in the retreat dates of NARS between the future SSP585 and historical simulations is statistically insignificant for majority of the models with only 6 models showing any significant difference (Fig. 23b). Consequently, the differences in the length of NARS are also insignificant in most of the models except 4 models (Fig. 23c). However, future change of seasonal rainfall of NARS is significant in 11 of the models, off which 9 of them indicate an increase under this socio-economic pathway.

The linear correlations of the onset and the retreat dates of NARS with seasonal length and seasonal rainfall anomaly for the SSP585 simulations in Table 3 show insignificant changes from the corresponding historical simulations. However, the correlations of the ENSO index with NARS parameters in the SSP585 simulations in Figs. 24a-d have changed from the historical simulations. For example, the correlations of the onset date with the ENSO index in Fig. 24a shows that nine models display negative correlations contrary to the relatively uniform positive correlations in the historical simulations (Fig. 22a). Similarly, the retreat date correlations with

ENSO index in the SSP585 simulations (Fig. 24b) show majority of models showing reduced negative correlations than the historical simulations (Fig. 22b) with some even showing positive correlations. As a result, the correlations of the length of NARS with the ENSO index in the SSP585 simulations (Fig. 24c) are less robust with many models showing insignificant values and even positive values in contrast to the historical simulation (Fig. 22c). Finally, the correlations of the seasonal rainfall anomaly of NARS with the ENSO index in the SSP585 simulations appear to be less uniform and weak across models (Fig. 24d) relative to the historical simulation (Fig. 22d). The disruption of the ENSO teleconnection with NARS in the SSP585 seems to stem from changes in ENSO variability as reported in (Fredriksen et al. 2020; Grose et al. 2020; Beobid-Arsuaga et al. 2021) given that the change in the mean climate of NARS in the SSP585 relative to the historical simulation is largely small (Figs. 23a-d),

Interestingly, most of the models show insignificant linear trends in the onset date (Fig. 25a), demise date (Fig. 25b), length of the season (Fig. 25c) and seasonal rainfall (Fig. 25d) of NARS. In Fig. 8a, the trend of the onset date of NARS is statistically significant in only four models. Three of these models show a negative trend, towards earlier onset and the one model (ACCESS-CM2) shows a positive trend of later onset date of NARS. Similarly, the linear trend of the retreat date (Fig. 25b), length of the season (Fig. 25c) and seasonal rainfall (Fig. 25d) of NARS is significant in only three, three and five models, respectively.

4.9 Future climate projections under SSP126

The SSP126 simulation is the sustainable, green pathway, wherein the CO2 concentration will reduce to about 425 ppm by the end of the 21st century, which is a drop from a peak of over 450 ppm in the mid-21st century. A comparison of the SSP126 and SSP585 projections is often

made to highlight the impact of the future socioeconomic pathways on the evolution of the end of the century climate (e.g., Grose et al. 2020, Beobide-Arsuaga et al. 2020).

We note that the climatological difference in the onset date (Fig. 26a), demise date (Fig. 26b), length of the season (Fig. 26c), and seasonal rainfall (Fig. 26d) between the future SSP126 and historical simulations in the majority of the CMIP6 models is insignificant. The change in the seasonal rainfall from 9 models (Fig. 26d) is the most followed by change in the demise date in 5 models (Fig. 26b). Interestingly, 6 of the 9 models display an increase in the seasonal rainfall and all 5 of the 5 models suggest an earlier retreat in the future climate relative to the historical simulation.

The correlations of the onset/retreat dates with the corresponding seasonal length and seasonal rainfall anomalies of NARS show insignificant differences from the historical or SSP585 simulations (not shown). However, the correlations of the onset date with the ENSO index in the SSP126 simulations (Fig. 27a) appear very similar with SSP585 simulations (Fig. 24a) and quite different from the historical simulations (Fig. 22a). Similarly, the retreat date (Fig. 10b), the length of the season (Fig. 27c), and the seasonal rainfall (Fig. 27d) correlations with the ENSO index in SSP126 simulations also show close resemblance to the corresponding SSP585 simulations (Figs. 24b-d), which is a deviation from the corresponding historical simulation results (Fig. 22b-d). Beobid-Arsuaga et al. (2021) found that the scenario uncertainty on ENSO projections was the least compared to uncertainty stemming from model and internal variability. These shrinking correlations between the NARS rainfall and ENSO suggest that the teleconnection between ENSO and the NARS becomes weaker in a future climate.

The linear trend of the onset date (Fig. 28a), retreat date (Fig. 28b), length of the season (Fig. 28c), and seasonal rainfall of NARS (Fig. 28d) under the SSP126 pathway is statistically

insignificant in a large majority of the models. This suggests in combination with similar conclusion about the linear trends from the SSP585 simulation, that the socioeconomic pathways may not have as significant of an impact on NARS.

CHAPTER 5

CONCLUSIONS

The local definition of NARS, as introduced in this paper, is an attractive complement to the aggregate evolution of NARS in UM20. The spatial heterogeneity observed in the evolution of the rainy season over northern Australia with early onsets and longer length of the season occurring to the west of Gulf of Carpentaria necessitates a local definition for the onset and the retreat of NARS.

The local definition of onset/retreat of NARS is based on daily rainfall analysis, which is defined at individual grid points. This definition requires a robust seasonal cycle of rainfall so that onset and retreat can be defined as the first and the last day of the year when the daily rain rate exceeds and falls below the climatological annual mean rain rate. However, to avoid false onset/retreat dates that are not associated with the rainy season, we anchor our local definition of onset/retreat to the climatological evolution of the local rainy season with respect to the corresponding aggregate NARS evolution. This local definition provides an unambiguous, objective definition of the onset/retreat of NARS defined locally, at the individual grid points of the rainfall analysis.

The proposed definition of local onset/retreat NARS has many advantages. Foremost it accounts for local variations in the length of the season, which is an important variant of the season. Secondly, it is based solely on rainfall, which makes it convenient to implement in case of real-time monitoring of the season. We tested this methodology over a century-long rainfall analysis, which showed the efficacy of this objective definition in providing unambiguous local onset/retreat dates throughout the period. In the future, this definition could be adopted on remotely sensed

rainfall products that are available on shorter periods of time at potentially higher spatial resolution and available in real-time. Furthermore, the introduced methodology for diagnosing local onset and retreat of NARS is easily adaptable to the available resolution of the rainfall analysis.

Our study finds that local onset/retreat variations have an implication on the corresponding length of the season and seasonal rainfall anomaly. We find that early or later local onset of the rainy season is associated with longer and wetter or shorter and drier seasons, respectively. This relationship can be exploited to provide a localized seasonal outlook of the rainy season by monitoring the local onset. Similarly, the linear relationship of the variations of the local retreat of the season with the corresponding length of the season and seasonal rainfall anomaly provides an understanding of the local evolution of the season posteriorly.

The frequency of the local onset and retreat of NARS is prominent in the wet and dry phases of the ISO, respectively. There is a far greater frequency of local demise (71.31%) during the dry spells of the ISO relative to the wet spells of the ISO. However, the frequency of local onset during wet spells of the ISO is 44.65%, which is less than the local onset occurring in the dry spells of the ISO. This observation is intriguing but nonetheless important to note, while future studies examine the subseasonal predictability of the evolution of NARS. The spatial distribution of the frequency of local demise of NARS during the various phases of the ISO exhibit coherent areas of high frequency during dry phases of ISO around the Gulf of Carpentaria. However, such spatial patterns are less discerning with regard to local onsets of NARS and ISO phases.

The ENSO teleconnections show that there is a strong relationship with the local variations of NARS. Early local onset, later local retreat, longer local length, and local wetter rainy season anomalies are associated with negative ENSO Niño3.4 SST anomalies. Likewise, later onset, early local retreat, shorter local length, and local drier rainy seasonal anomalies are associated with

positive ENSO SST anomalies. These teleconnections exhibit some spatial heterogeneity, with the eastern part of northern Australia exhibiting stronger correlations with ENSO Niño3.4 SST anomalies than the regions to the west of 140°E. Furthermore, in comparison to the fixed-length seasonal rainfall anomalies of DJF, the correlations with ENSO Niño3.4 SST anomalies with locally varying length of NARS rainfall anomalies display a stronger and more widespread correlation to the west of 140°E over northern Australia. This suggests that the seasonal predictability of NARS with a variable seasonal length in relation to its variation with ENSO could be potentially exploited further than by using a fixed-length season of NARS.

Our study reveals that a majority of CMIP6 models display a reasonable seasonal evolution of NARS with a reasonable climatology. For example, most historical simulations of CMIP6 models display a bias of ~ 10-15 days in their onset and retreat dates and in the length of the season. However, there are other variables like the seasonal rainfall of NARS for which CMIP6 historical simulations display significant bias ranging between -100mm to 900mm. Furthermore, the robust linear trends in onset and retreat dates, length of the season and seasonal rainfall of NARS found in the observations is unmatched by any of the historical simulations of CMIP6 models. But it is encouraging to note that the interannual variations of the onset date, retreat date, length, and seasonal rainfall of NARS is very well replicated by all models including their teleconnection with ENSO.

The future climate projections both under SSP585 (fossil fueled) and SSP126 (sustainable green) socioeconomic pathway indicate insignificant change of climatological mean onset date, retreat date, length, and seasonal rainfall of NARS from the historical simulation in most of the CMIP6 models. In terms of interannual variations, we observe that ENSO teleconnection with NARS is disrupted in the future climate under both extreme socio-economic pathways. However,

the inter-relationships between onset, retreat dates, seasonal length and seasonal rainfall are maintained in the future climate. The linear trends of the onset date, retreat date, length, and seasonal rainfall of NARS under both the future scenarios are also insignificant in most of the CMIP6 models. These results suggest that the greenhouse emissions do not seem to have a significant impact on NARS, in at least a majority of the CMIP6 models examined in this study. The changes in the ENSO teleconnection with NARS stems from changes in ENSO in the future climate as reported in (Fredriksen et al. 2020; Grose et al. 2020; Beobid-Arsuaga et al. 2021).

APPENDIX A

TABLES

Table 1: Brief details of the CMIP6 models used in this study

Model	Runs	Atmospheric Resolution (°)	Oceanic Resolution (°)	Climate Sensitivity (°C)
ACCESS-CM2	Historical, SSP126, SSP585	1.2 X 1.8	1.0 X 0.7	4.7
ACCESS-ESM1-5	Historical, SSP126, SSP585	1.2 X 1.8	1.0 X 0.7	3.9
BCC-CSM2-MR	Historical, SSP126, SSP585	1.1 X 1.1	1.0 X 0.7	3.1
CAMS-CSM1-0	Historical, SSP126, SSP585	1.1 X 1.1	1.1 X 1.1	2.3
CESM2	Historical, SSP126, SSP585	0.9 X 1.3	1.1 X 0.4	5.2
CESM2-WACCM	Historical, SSP585	0.9 X 1.3	0.9 X 1.3	4.7
CNRM-CM6-1	Historical, SSP126, SSP585	1.4 X 1.4	1.0 X 0.8	4.8
CNRM-CM6-1-HR	Historical, SSP126, SSP585	0.5 X 0.5	0.25 X 0.25	8.8
CNRM-ESM2-1	Historical, SSP126	1.4 X 1.4	1.0 X 0.8	4.8
EC-Earth3	Historical, SSP126	0.7 X 0.7	1.0 X 0.8	4.2
EC-Earth3-Veg	Historical, SSP126, SSP585	0.7 X 0.7	1.0 X 0.8	4.3

FGOALS-g3	Historical, SSP126, SSP585	2.3 X 2.0	2.3 X 2.0	2.8
GFDL-CM4	Historical, SSP585	1.0 X 1.3	0.3 X 0.2	3.9
GFDL-ESM4	Historical, SSP126, SSP585	1.0 X 1.3	0.5 X 0.5	2.7
INM-CM4-8	Historical, SSP126, SSP585	1.5 X 2.0	1.0 X 0.5	1.8
INM-CM5-0	Historical, SSP126, SSP585	1.5 X 2.0	1.0 X 0.5	1.9
IPSL-CM6A-LR	Historical, SSP126, SSP585	1.3 X 2.5	1.0 X 0.8	4.5
MIROC-ES2L	Historical, SSP126, SSP585	2.7 X 2.8	1.0 X 0.7	2.7
MPI-ESM1-2-HR	Historical, SSP126, SSP585	0.9 X 0.9	0.4 X 0.4	3
MPI-ESM1-2-LR	Historical, SSP126, SSP585	2.0 X 2.0	0.4 X 0.4	3.5
MRI-ESM2-0	Historical, SSP126, SSP585	1.1 X 1.1	1.1 X 1.1	3.2
NESM3	Historical, SSP126, SSP585	1.9 X 1.9	1.0 X 0.8	4.7
NorESM2-LM	Historical, SSP126, SSP585	1.9 X 2.5	1.0 X 0.5	2.5
NorESM2-MM	Historical, SSP126, SSP585	0.25 X 0.25	0.25 X 0.25	2.5

Table 2: The correlations of the various parameters of the northern Australian Rainy Season from observations and historical simulations of the CMIP6 models (after removing linear trends). Significant values at 95% significance level are in bold

Model	Onset vs Demise dates	Onset date vs seasonal length	Onset date vs seasonal rainfall anomaly	Demise date vs seasonal length	Demise date vs seasonal rainfall anomaly	Seasonal length vs seasonal rainfall anomaly
ACCESS-CM2	-0.14	**-0.70**	**-0.61**	**0.80**	**0.53**	**0.75**
ACCESS-ESM1-5	**-0.16**	**-0.76**	**-0.65**	**0.77**	**0.60**	**0.82**
BCC-CSM2-MR	-0.04	**-0.63**	**-0.55**	**0.80**	**0.47**	**0.69**
CAMS-CSM1-0	-0.05	**-0.58**	**-0.52**	**0.84**	**0.47**	**0.66**
CESM2	**-0.16**	**-0.79**	**-0.70**	**0.73**	**0.54**	**0.82**
CESM2-WACCM	**-0.20**	**-0.80**	**-0.71**	**0.75**	**0.56**	**0.82**
CNRM-CM6-1	-0.01	**-0.66**	**-0.49**	**0.76**	**0.50**	**0.70**
CNRM-CM6-1-HR	0.07	**-0.62**	**-0.35**	**0.74**	**0.38**	**0.54**
CNRM-ESM2-1	-0.05	**-0.66**	**-0.52**	**0.78**	**0.49**	**0.69**
EC-Earth3	0.08	**-0.71**	**-0.35**	**0.64**	**0.51**	**0.62**
EC-Earth3-Veg	-0.10	**-0.77**	**-0.47**	**0.70**	**0.47**	**0.64**
FGOALS-g3	0.01	**-0.73**	**-0.61**	**0.67**	**0.49**	**0.78**
GFDL-CM4	**-0.19**	**-0.79**	**-0.55**	**0.75**	**0.58**	**0.73**
GFDL-ESM4	-0.09	**-0.74**	**-0.46**	**0.74**	**0.54**	**0.68**
INM-CM4-8	-0.11	**-0.74**	**-0.43**	**0.75**	**0.61**	**0.70**
INM-CM5-0	-0.06	**-0.73**	**-0.45**	**0.72**	**0.54**	**0.68**
IPSL-CM6A-LR	-0.11	**-0.83**	**-0.64**	**0.65**	**0.58**	**0.82**
MIROC-ES2L	**-0.16**	**-0.76**	**-0.58**	**0.77**	**0.51**	**0.71**
MPI-ESM1-2-HR	-0.15	**-0.80**	**-0.55**	**0.71**	**0.46**	**0.67**
MPI-ESM1-2-LR	0.04	**-0.80**	**-0.59**	**0.57**	**0.36**	**0.70**
MRI-ESM2-0	-0.11	**-0.77**	**-0.57**	**0.72**	**0.28**	**0.58**
NESM3	-0.04	**-0.69**	**-0.48**	**0.74**	**0.62**	**0.76**
NorESM2-LM	**-0.19**	**-0.77**	**-0.72**	**0.77**	**0.60**	**0.85**
NorESM2-MM	**-0.21**	**-0.83**	**-0.72**	**0.70**	**0.53**	**0.83**
Observations	-0.18	**-0.75**	**-0.65**	**0.79**	**0.41**	**0.68**

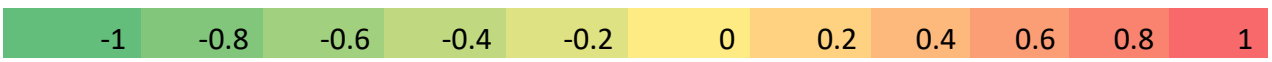

Table 3: The correlations of the various parameters of the northern Australian Rainy Season from SSP585 simulation of the CMIP6 models (after removing linear trends). Significant values at 95% significance level are in bold

Model	Onset vs Demise dates	Onset date vs seasonal length	Onset date vs seasonal rainfall anomaly	Demise date vs seasonal length	Demise date vs seasonal rainfall anomaly	Seasonal length vs seasonal rainfall anomaly
ACCESS-CM2	-0.03	**-0.67**	**-0.52**	**0.75**	**0.32**	**0.59**
ACCESS-ESM1-5	**-0.24**	**-0.66**	**-0.57**	**0.88**	**0.65**	**0.78**
BCC-CSM2-MR	**-0.35**	**-0.79**	**-0.59**	**0.85**	**0.64**	**0.75**
CAMS-CSM1-0	0.01	**-0.41**	**-0.47**	**0.91**	**0.57**	**0.72**
CESM2-WACCM	**-0.24**	**-0.84**	**-0.75**	**0.73**	**0.57**	**0.85**
CESM2	**-0.36**	**-0.83**	**-0.81**	**0.81**	**0.64**	**0.88**
CNRM-CM6-1-HR	0.02	**-0.56**	**-0.31**	**0.81**	**0.34**	**0.46**
CNRM-CM6-1	**-0.28**	**-0.78**	**-0.55**	**0.82**	**0.52**	**0.66**
EC-Earth3-Veg	**-0.29**	**-0.74**	**-0.50**	**0.81**	**0.73**	**0.79**
FGOALS-g3	**-0.27**	**-0.78**	**-0.74**	**0.81**	**0.53**	**0.81**
GFDL-CM4	**-0.37**	**-0.89**	**-0.70**	**0.73**	**0.65**	**0.82**
GFDL-ESM4	-0.08	**-0.73**	**-0.56**	**0.73**	**0.55**	**0.76**
INM-CM4-8	-0.10	**-0.73**	**-0.49**	**0.72**	**0.59**	**0.75**
INM-CM5-0	-0.17	**-0.81**	**-0.53**	**0.72**	**0.61**	**0.74**
IPSL-CM6A-LR	-0.15	**-0.86**	**-0.61**	**0.64**	**0.56**	**0.77**
MIROC-ES2L	**-0.36**	**-0.85**	**-0.72**	**0.79**	**0.63**	**0.82**
MPI-ESM1-2-HR	0.03	**-0.74**	**-0.43**	**0.64**	**0.34**	**0.56**
MPI-ESM1-2-LR	**-0.27**	**-0.90**	**-0.65**	**0.66**	**0.47**	**0.72**
MRI-ESM2-0	-0.20	**-0.79**	**-0.54**	**0.76**	**0.49**	**0.67**
NESM3	**-0.23**	**-0.79**	**-0.53**	**0.76**	**0.43**	**0.63**
NorESM2-LM	-0.16	**-0.80**	**-0.80**	**0.71**	**0.51**	**0.88**
NorESM2-MM	0.01	**-0.84**	**-0.69**	**0.54**	**0.41**	**0.80**

APPENDIX B

FIGURES

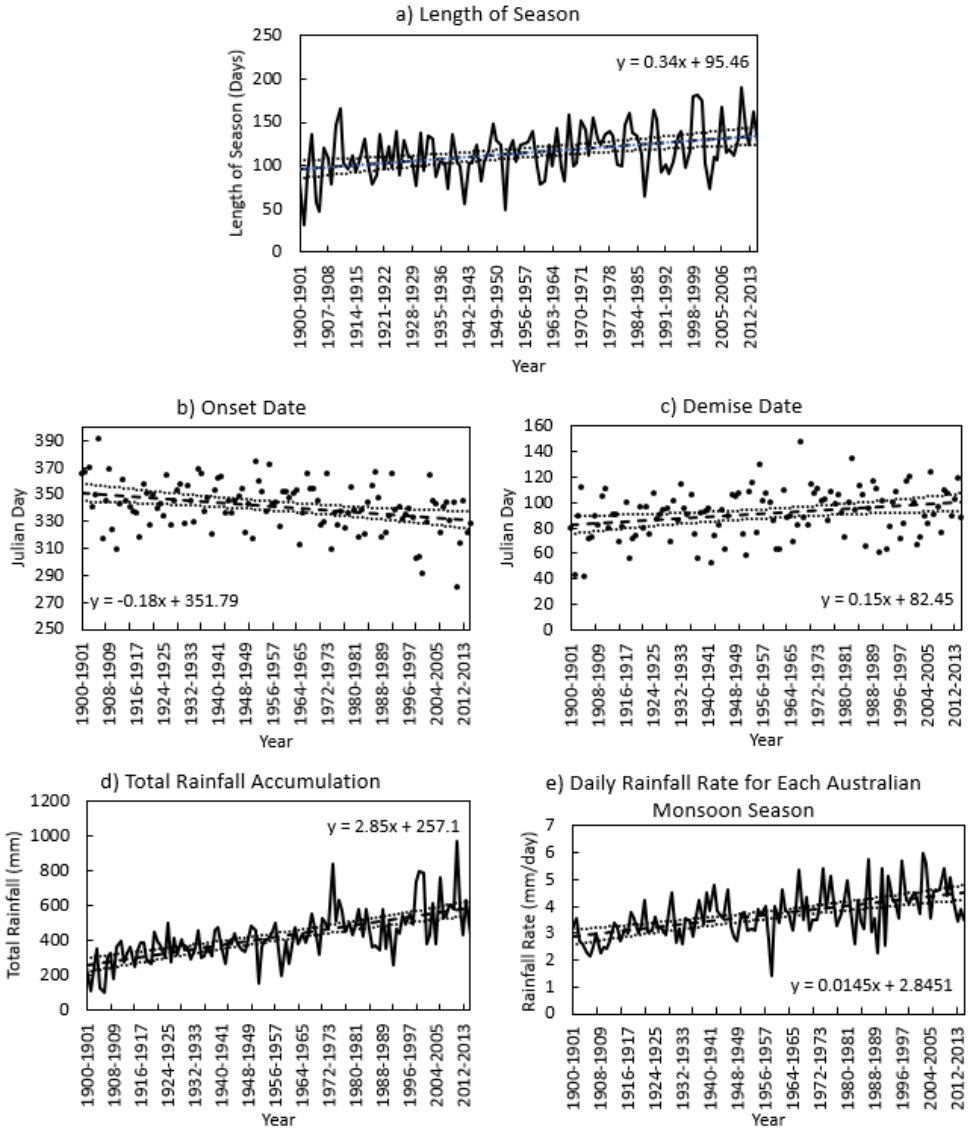

Figure 1: a) Length (days), b) onset (Julian) day, c) demise (Julian) day d) seasonal accumulation of rainfall (mm), and e) mean seasonal rain rate (mm day^{-1}) of the aggregate northern Australian rainy season. The least squares fit line (dashed line) is overlaid with 95% confidence interval (dotted lines). The slope of the regression line is indicated in the figure with appropriate units. From Uehling and Misra (2020).

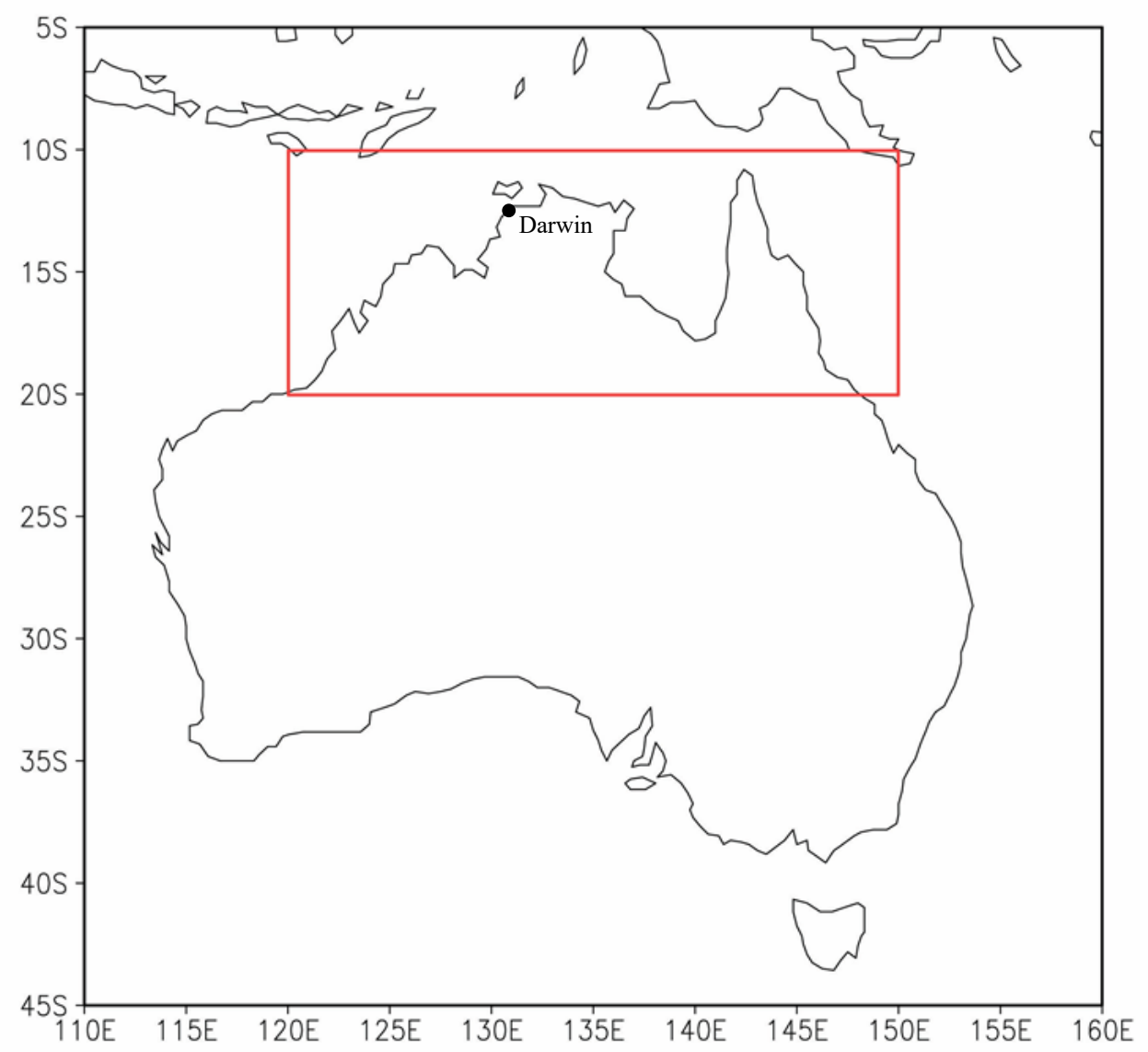

Figure 2: The domain highlighted in red is used to define the northern Australia Rainy Season (NARS).

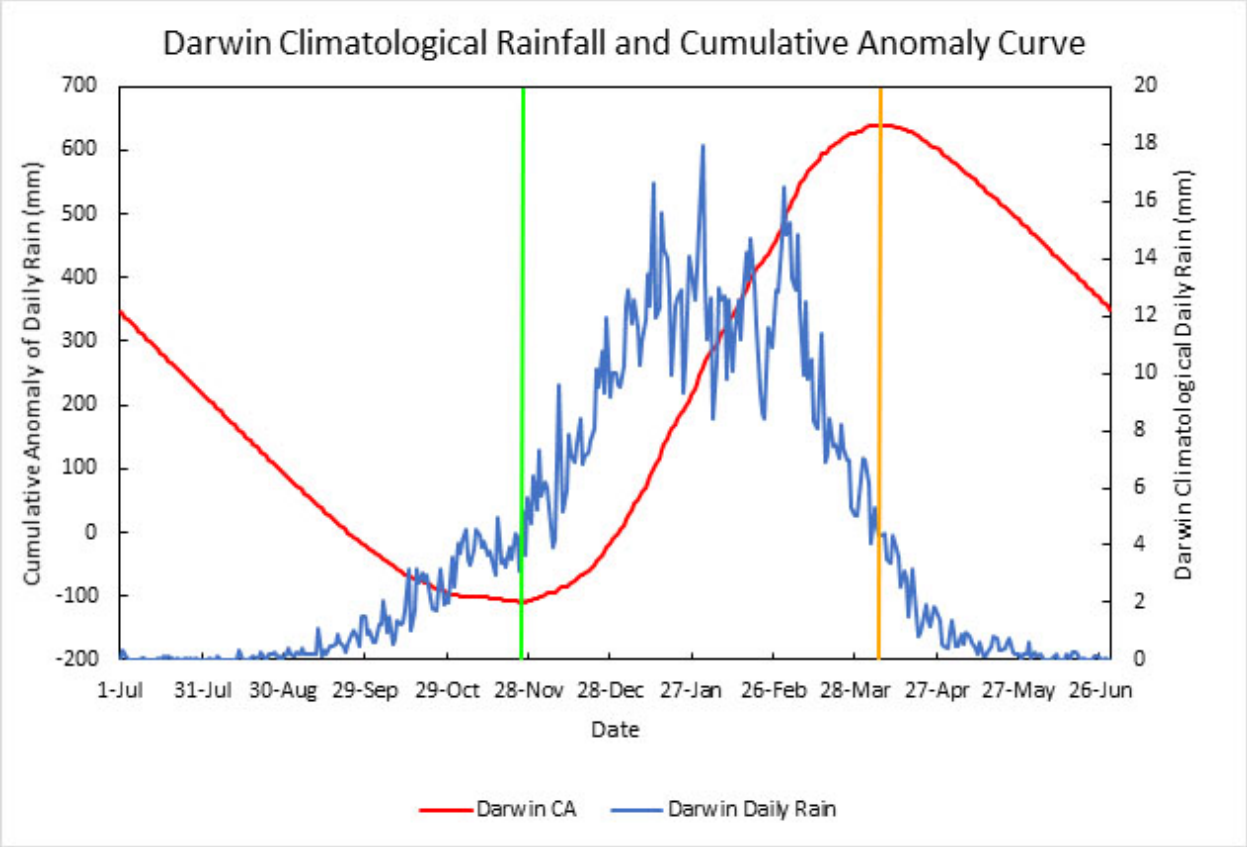

Figure 3: Daily climatological rain rate (in blue) over Darwin (12.4°S and 130.8°E). The corresponding daily cumulative anomaly of rainfall (in red) and the diagnosed onset (indicated by the green vertical line), and demise (indicated by the orange vertical line) dates are diagnosed by the minimum and maximum in the red curve, respectively.

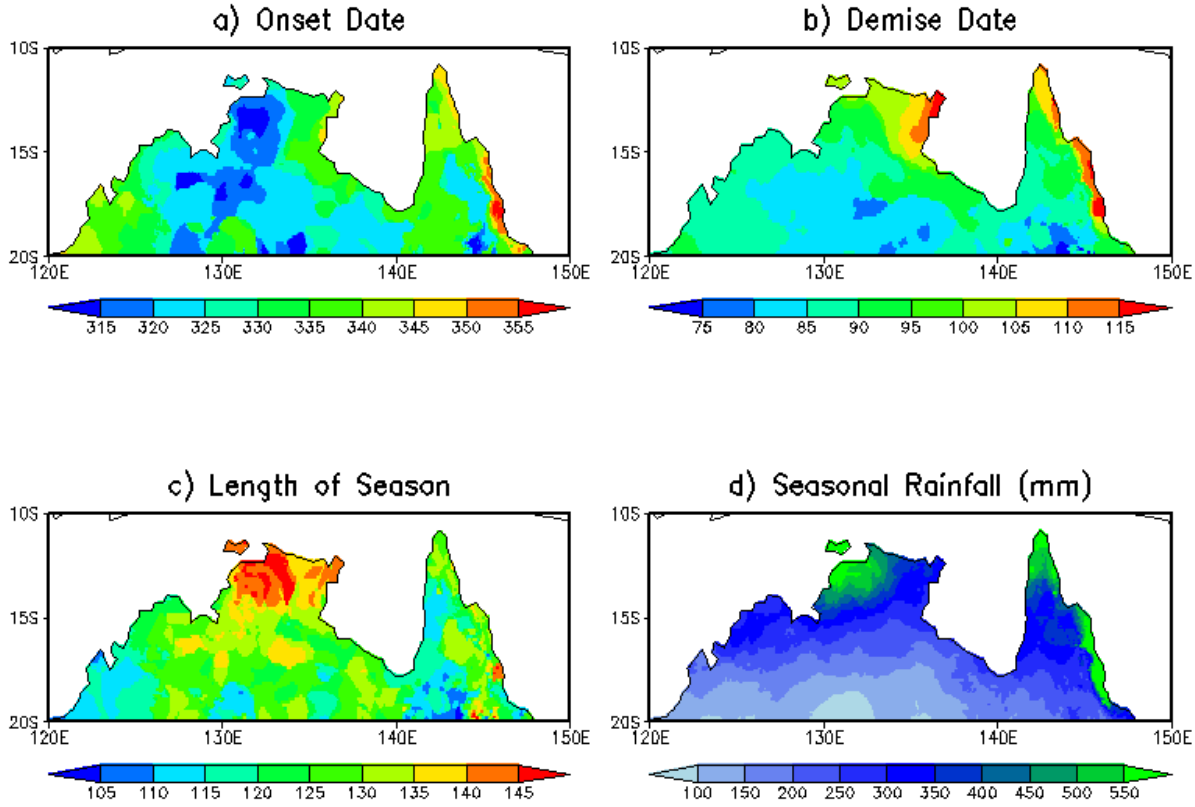

Figure 4: The climatological a) onset and b) demise date (in Julian days), and c) length (in days) of the NARS defined at every grid point of the Australian Bureau of Meteorology gridded rainfall dataset at 0.5° grid interval (Grant 2012). d) The climatological seasonal mean rainfall (mm), accumulated between the climatological local onset and demise date of the NARS at each grid point.

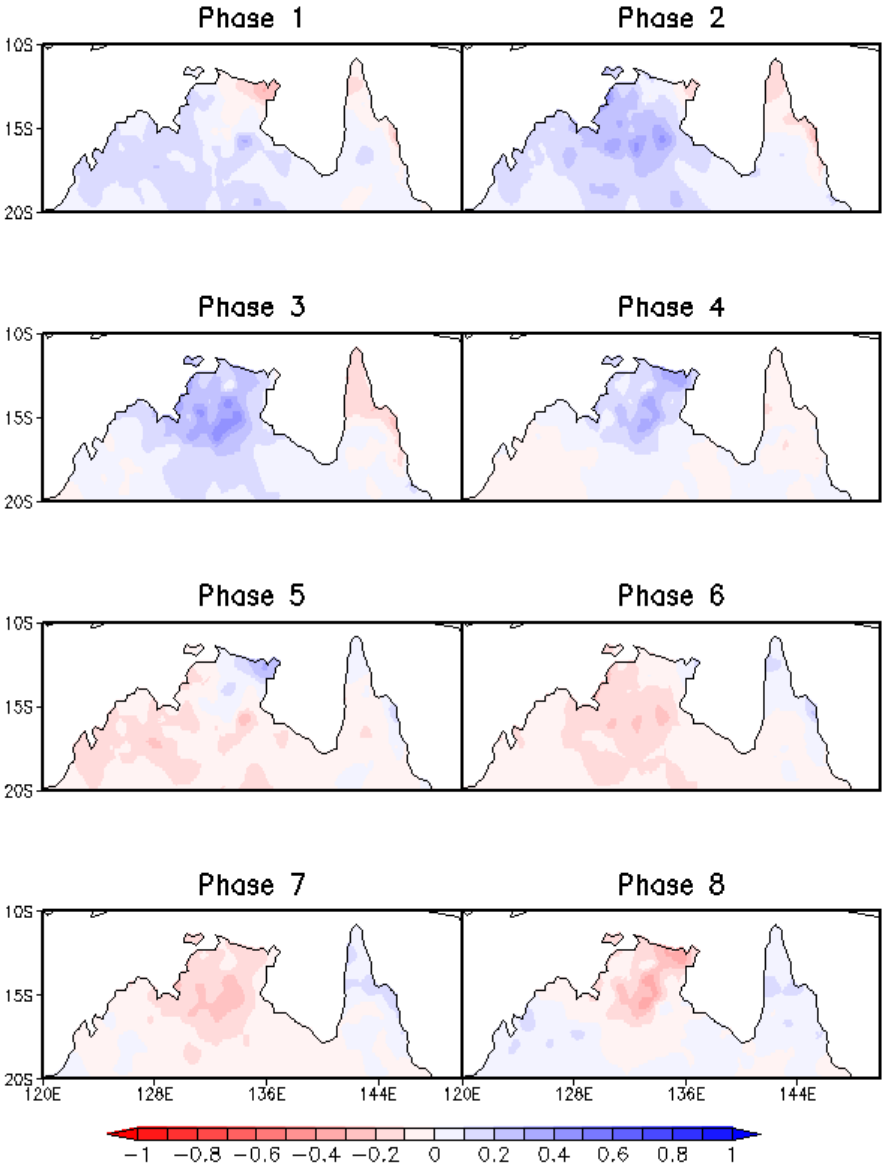

Figure 5: Phase composite diagram of the northern Australian monsoon for the 2014-2015 monsoon season.

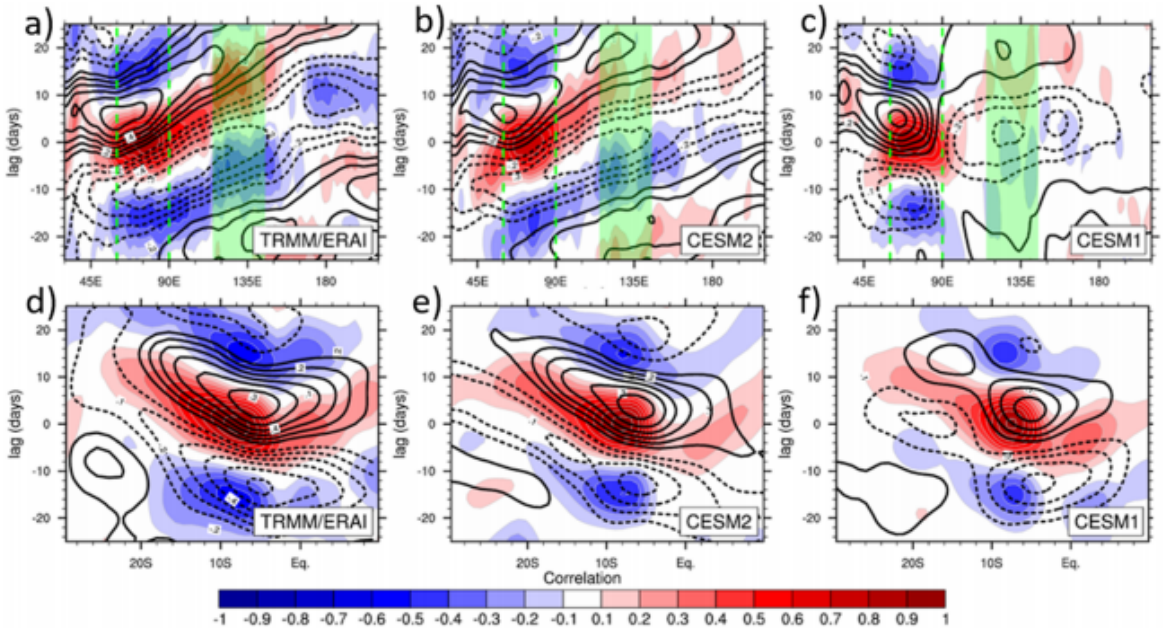

Figure 6: MJO signature over the northern Australian region as diagnosed by Meehl et al. 2020. Panels a,b, and c show the eastward propagation of the MJO with effects on the Australian monsoon, intraseasonal lag correlations of precipitation averaged between 60°E and 90°E shown using the green dashed lines, with precipitation (blue to red colored regions) and 850 hPa zonal wind (black lines) at longitudes in the indo-Pacific region (1998–2009) for observational data, CESM2, and CESM1 respectively. The green shaded regions show the Australian monsoon region. Panels d,e, and f show the same as a,b, and c respectively, but for the meridional propagation between 10°N and 20°S. Figure reproduced from Meehl et al. (2020).

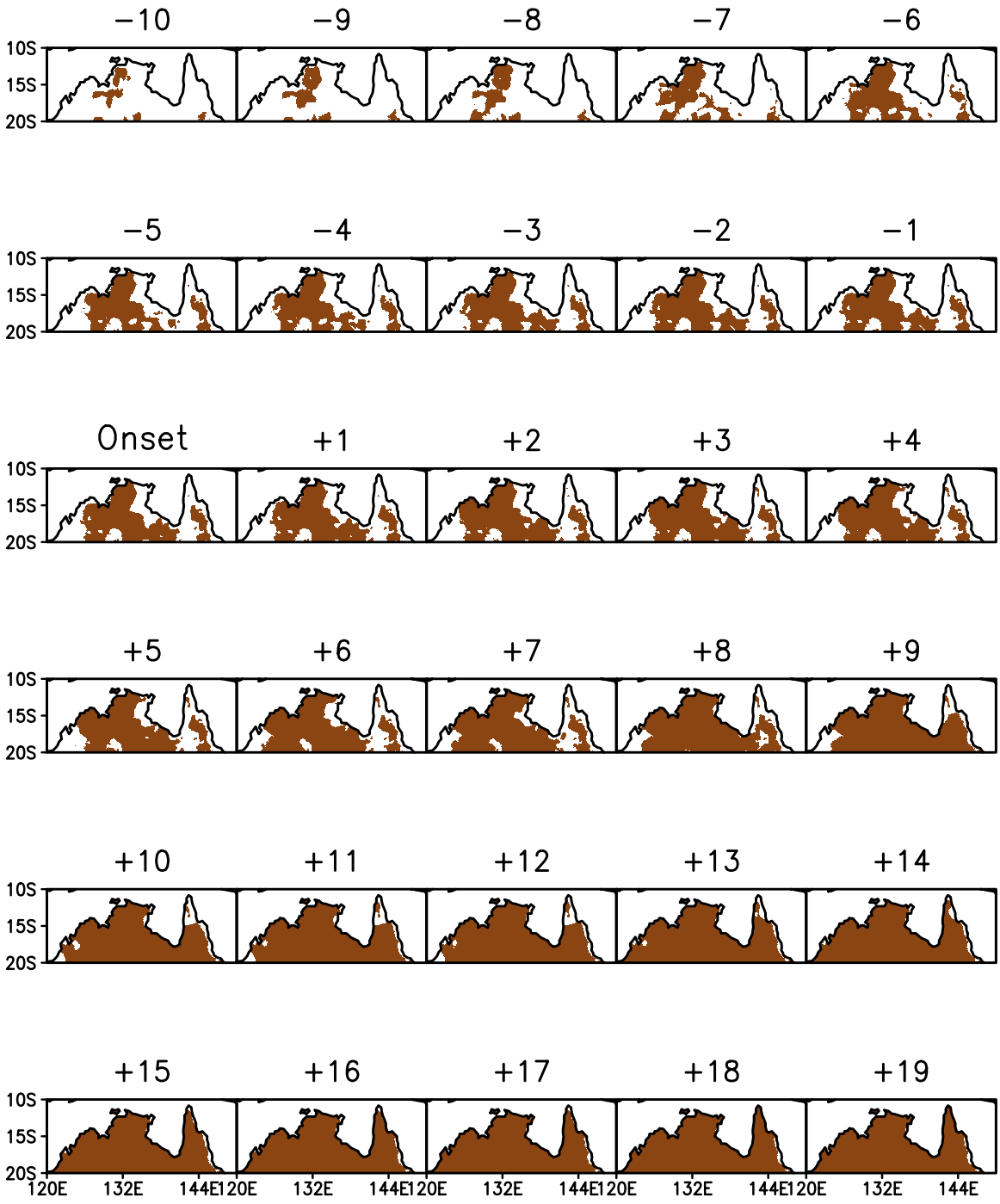

Figure 7: The progression of the climatological local onset date of the rainy season shown in brown from 10 days prior and 19 days post the aggregate NARS climatological onset date. The grid point is marked brown if the climatological local onset of the rainy season has occurred.

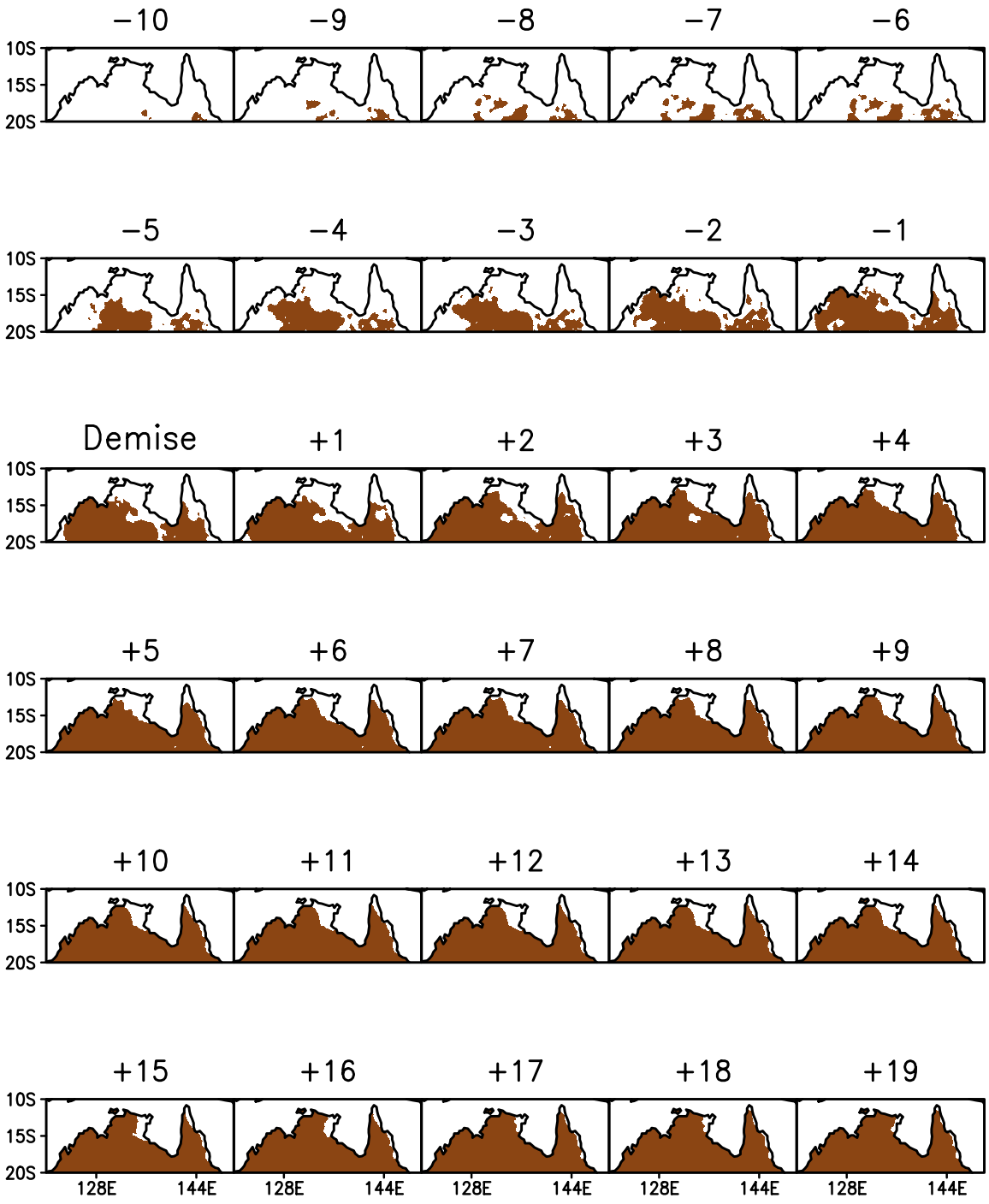

Figure 8: The progression of the climatological local demise date of the rainy season shown in brown from 10 days prior and 19 days post the aggregate NARS climatological demise date. The grid point is marked brown if the climatological local demise of the rainy season has occurred.

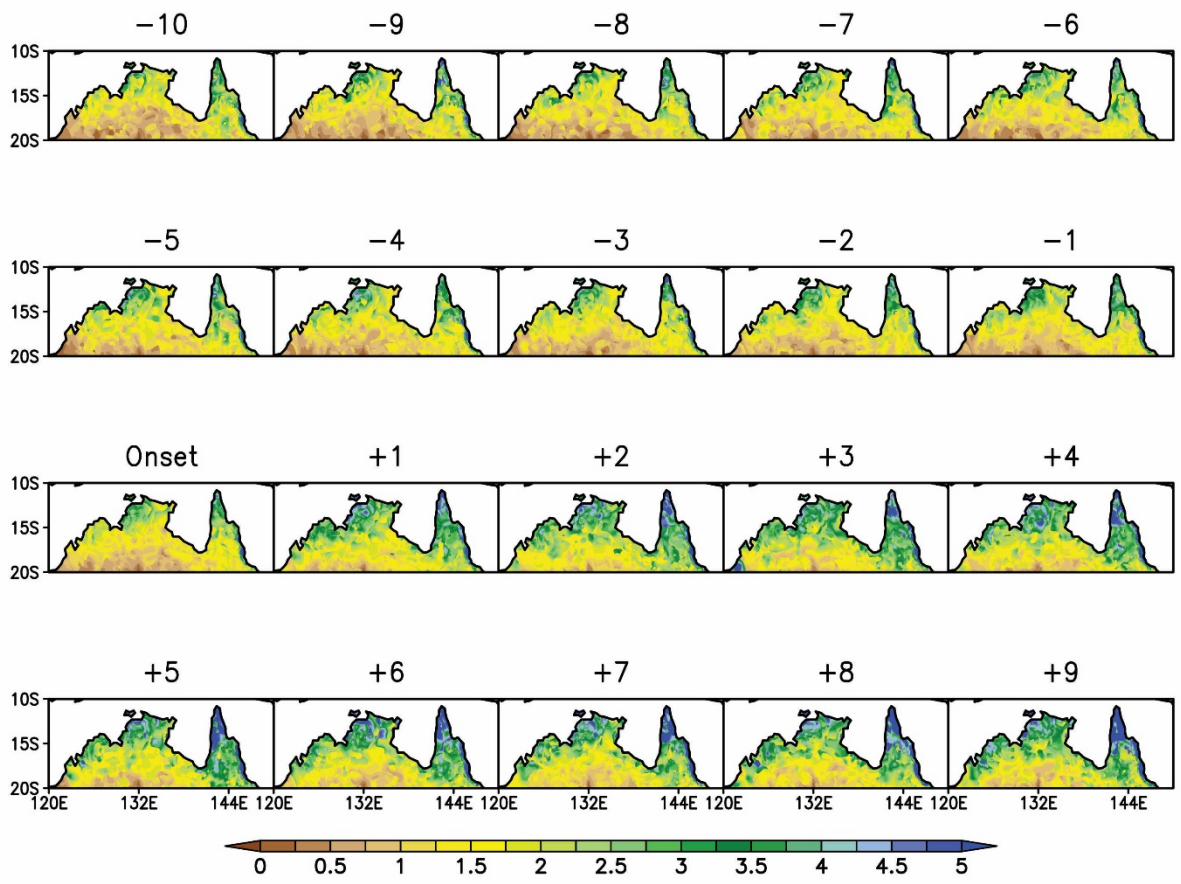

Figure 9: The climatological daily rainfall (mm day^{-1}) from 10 days prior to the time of local onset (0) to 9 days after the local onset date of NARS.

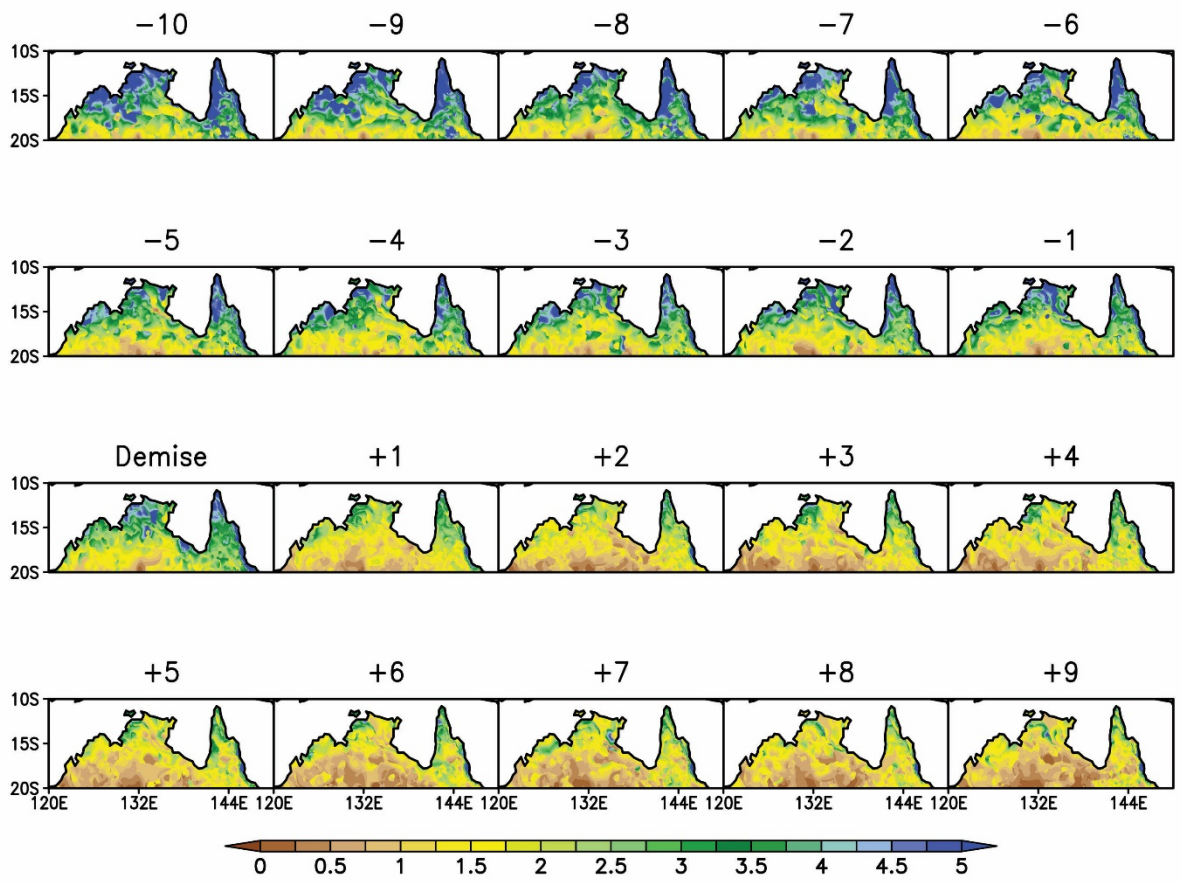

Figure 10: The climatological daily rainfall (mm day^{-1}) from 10 days prior to the time of local demise (0) to 9 days after the local demise date of NARS.

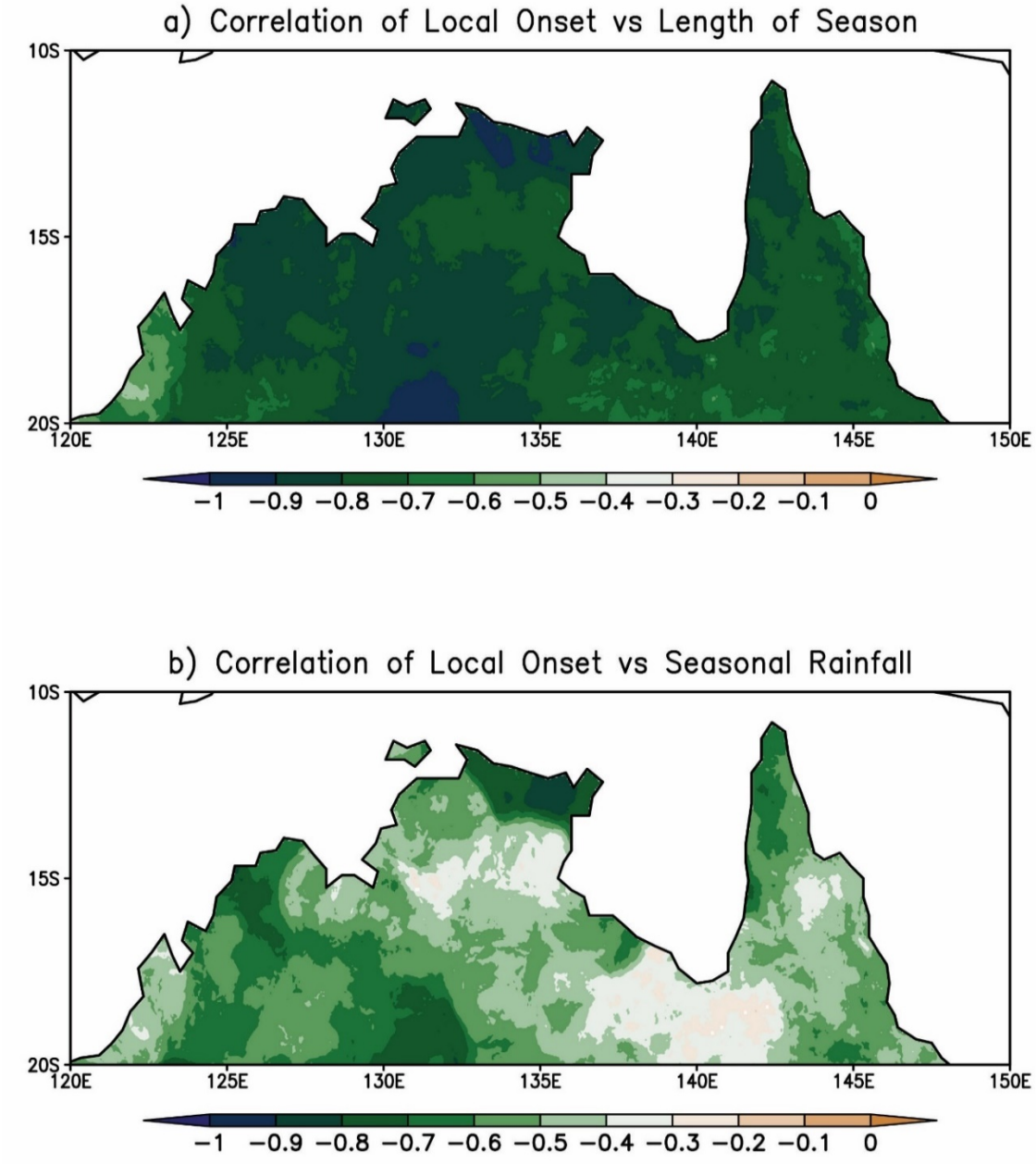

Figure 11: The correlation of the local onset date of NARS with corresponding a) local length of the NARS and b) local seasonal rainfall anomaly of NARS. Only significant values at 5% significance level by the bootstrap method are shaded.

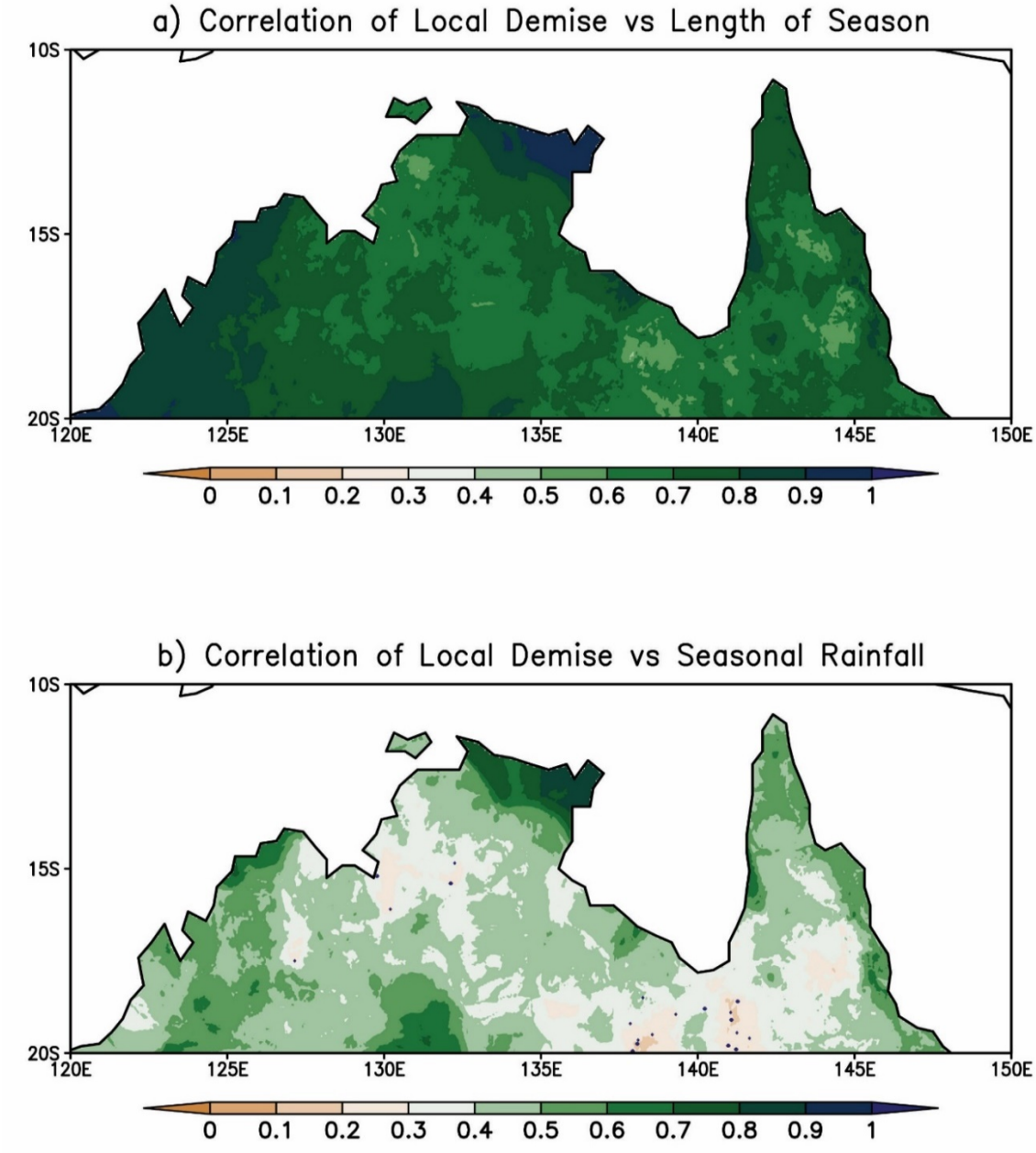

Figure 12: The correlation of the local demise date of the NARS with corresponding a) local length of the NARS, b) local seasonal rainfall anomaly. Only significant values at 5% significance level by the bootstrap method are shaded.

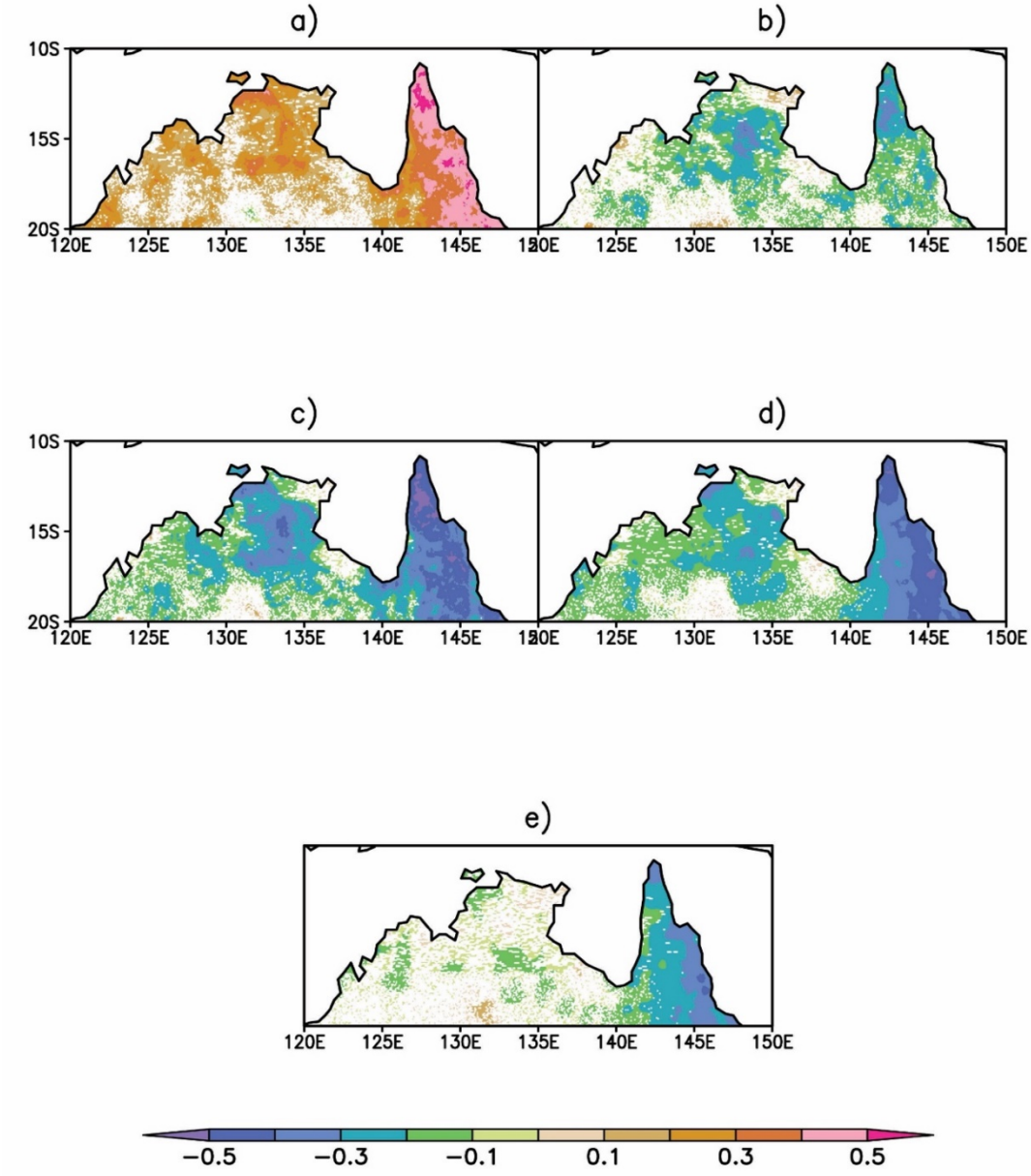

Figure 13: The correlation of September-October-November (SON) seasonal mean Niño3.4 (ENSO) SST anomalies with a) local onset date, b) local demise date, c) local seasonal length, d) local seasonal rainfall anomalies, and e) fixed length December-January-February (DJF) seasonal rainfall anomalies of NARS. All correlations significant at 95% confidence interval according to the bootstrap method are shaded.

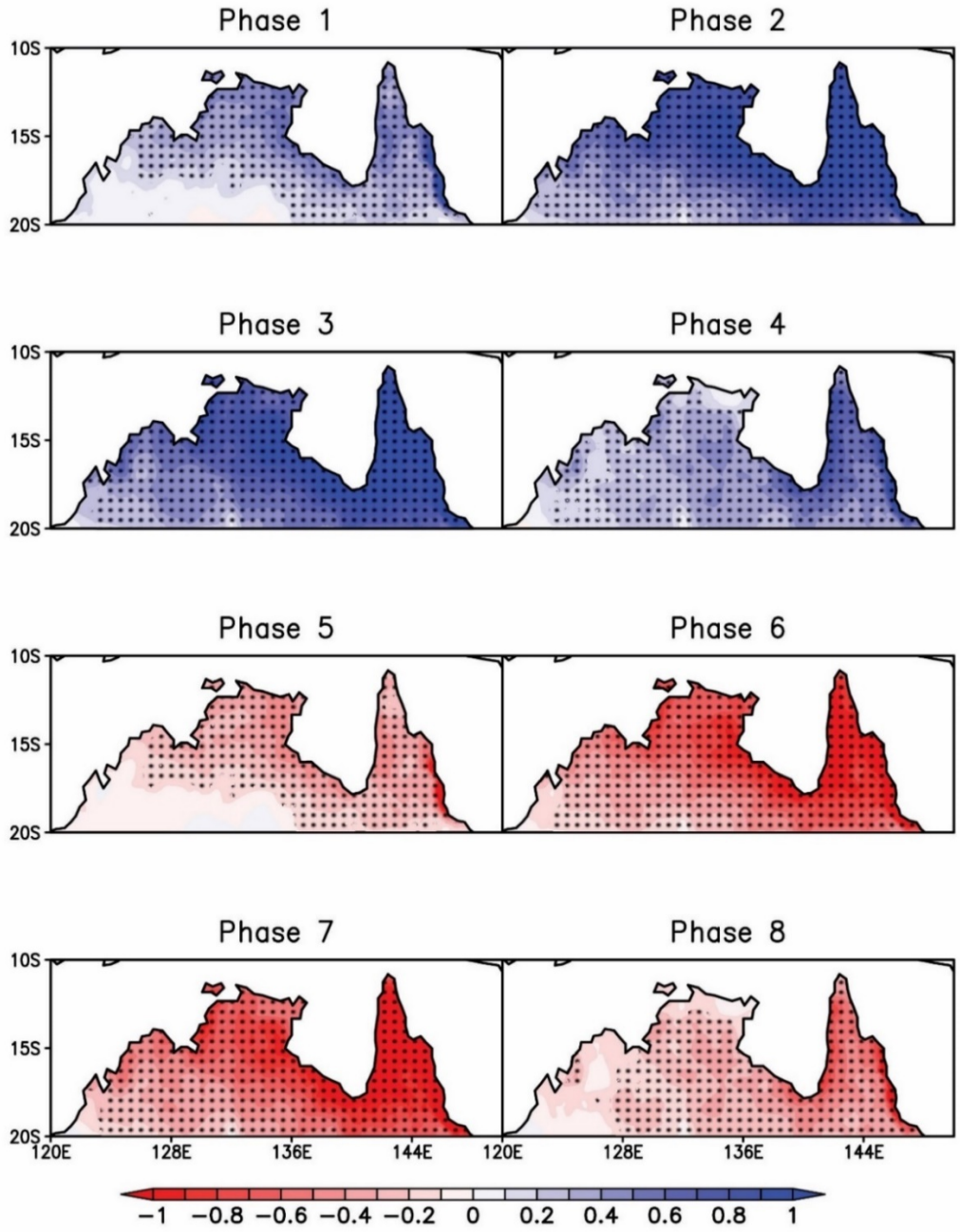

Figure 14: Composite rainfall anomalies (mm/day) for the 8 distinct phases of the ISO during November-May over the time period of 1900-2015 over northern Australia. The 8 phases of ISO were isolated from daily rainfall over northern Australia, as described in the text. Numbers in each panel show the corresponding phase number of the ISO. The stippled regions indicate values are significant at 5% significance level by the bootstrapping method.

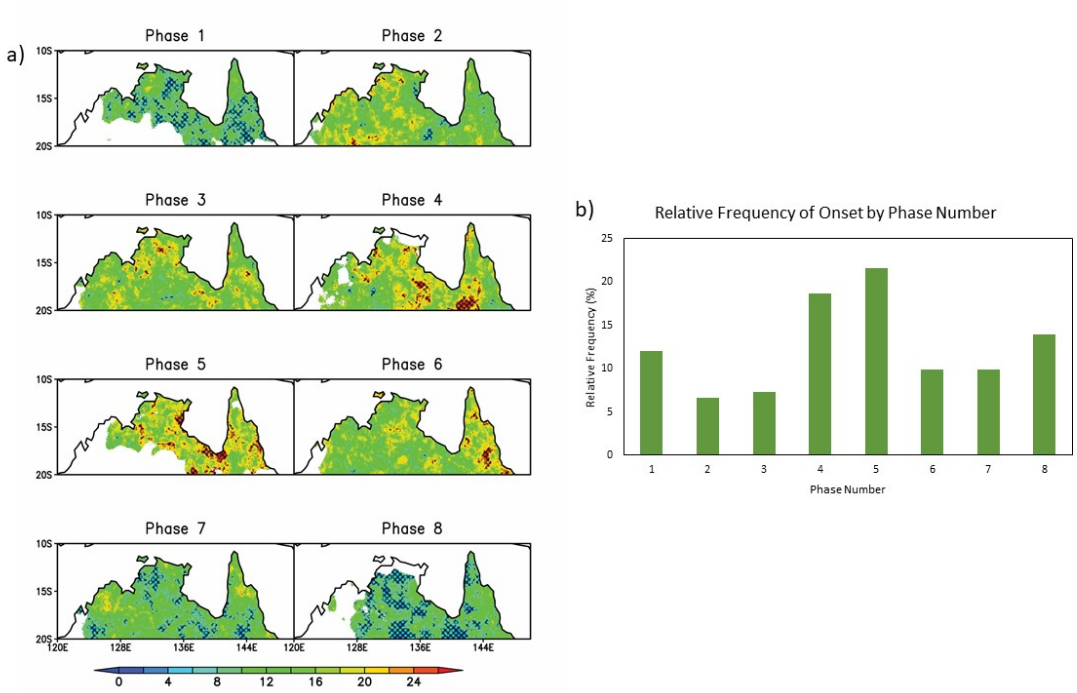

Figure 15: a) Spatial distribution of the frequency of local onset dates of NARS occurring in of the eight phases of ISO across northern Australia. The hatched regions indicate statistically significance at 5% significance level by the bootstrap method. b) Histogram showing the relative frequency (percentage) of local onset dates of NARS occurring during each phase of the ISO. The frequency is computed only in statistically significant regions (hatched regions in Figure 7a).

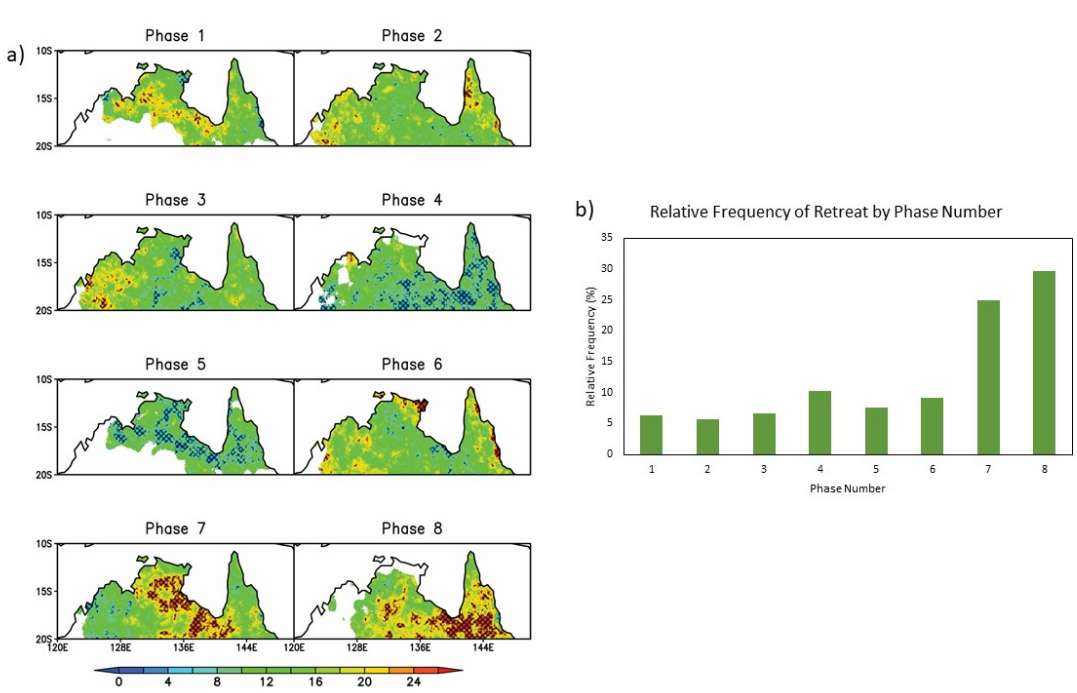

Figure 16: a) Spatial distribution of the frequency of local retreat dates of NARS occurring in each phase of the ISO across northern Australia. The hatched regions indicate statistically significance at 5% significance level by the bootstrap method. b) Histogram showing the relative frequency (percentage) of local retreat dates of NARS occurring during each phase of the ISO. The frequency is computed only in statistically significant regions (hatched regions in Figure 8a).

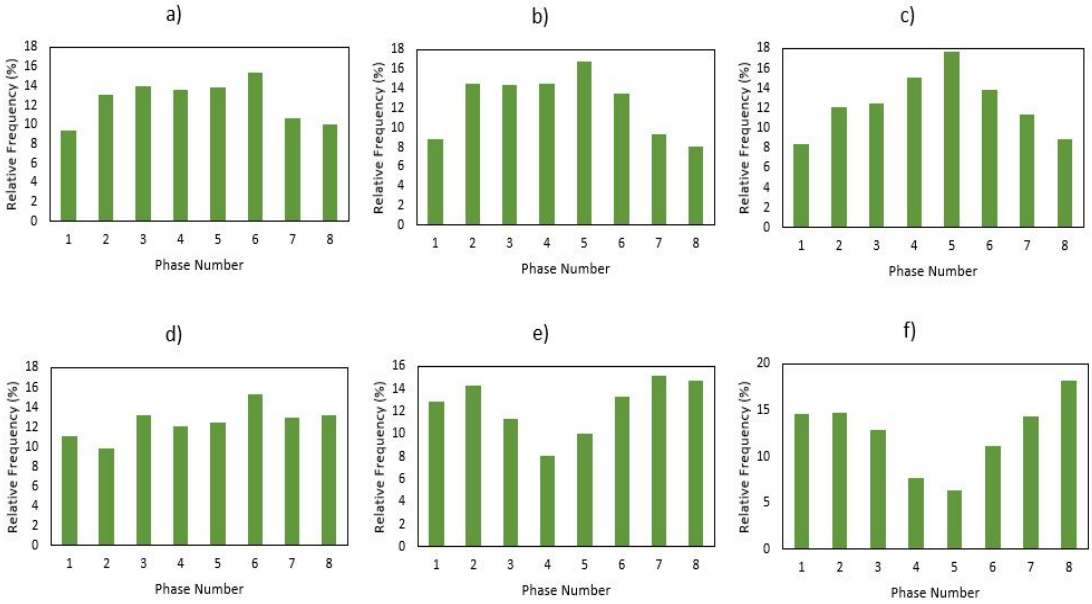

Figure 17: Histogram of the relative frequency (percentage) of local onset (a, b, and c) and demise (d, e, and f) dates of NARS occurring during each phase of the ISO for ENSO phases of La Niña (a and d), neutral (b and e), and El Niño (c and f).

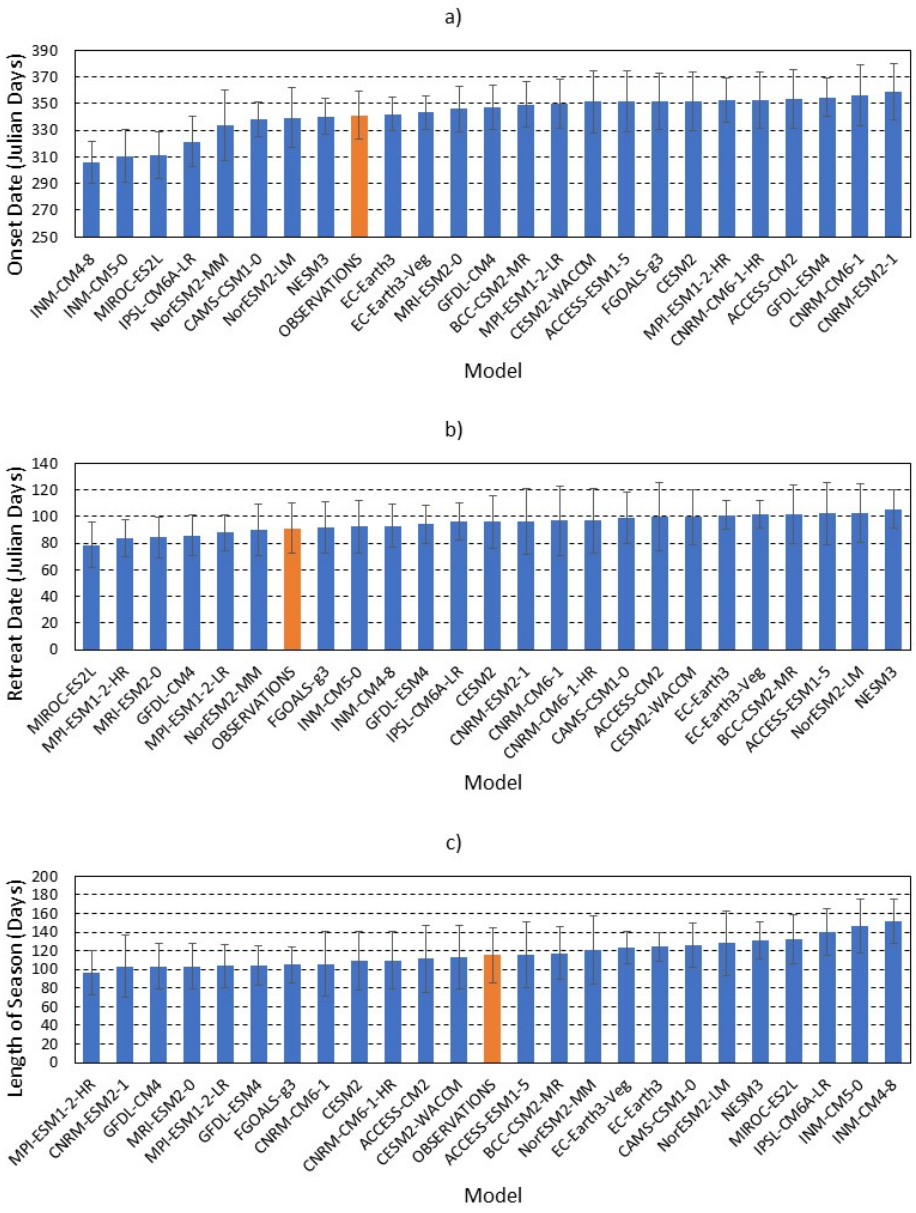

Figure 18: The climatological a) onset and b) retreat dates (in Julian days) and c) the length of NARS (in days) with the corresponding standard deviation shown in whiskers from the historical simulation of the CMIP6 models and observations (in orange).

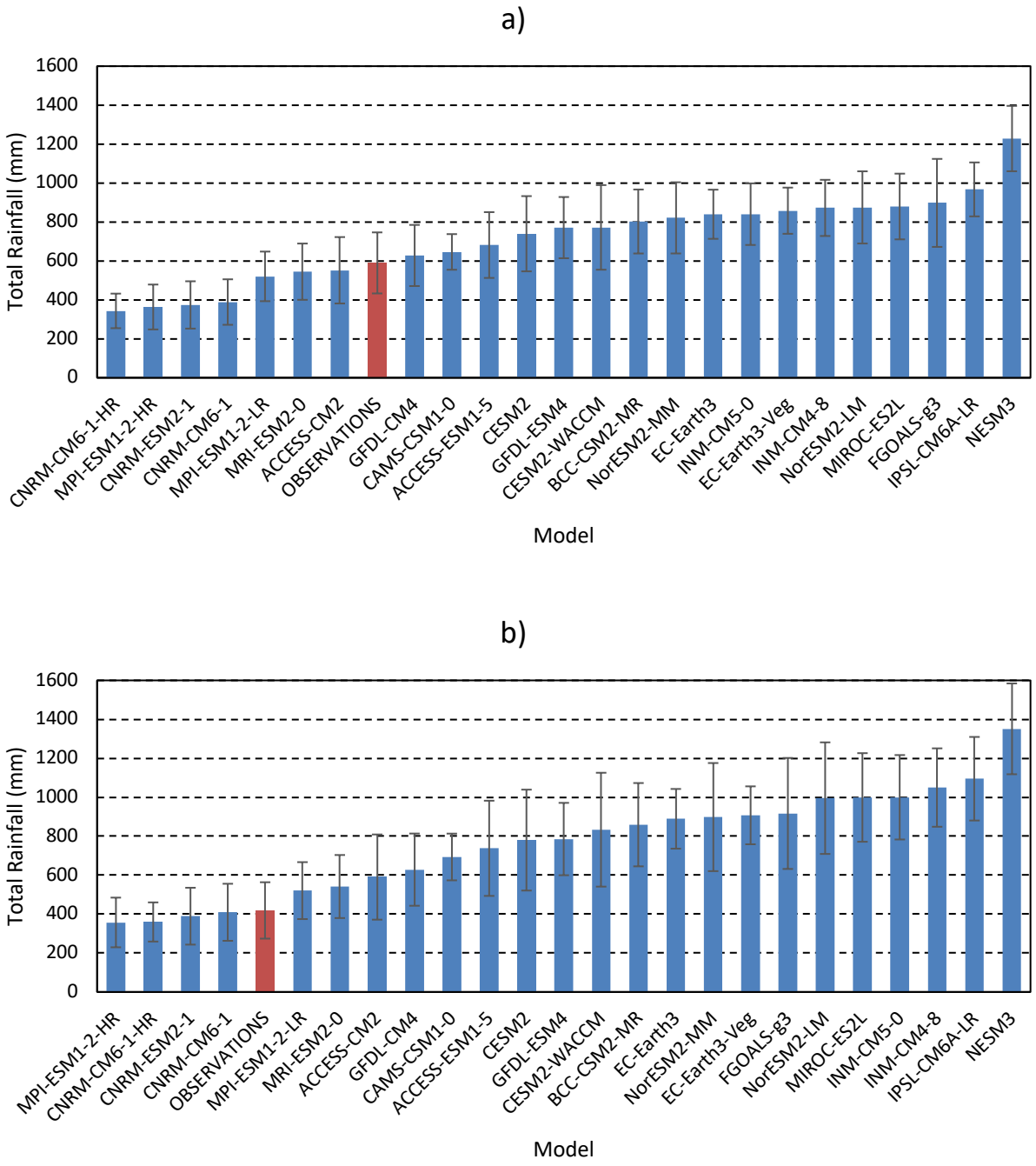

Figure 19: The climatological seasonal rainfall (mm day^{-1}) for a) fixed length (December-January-February) season and b) varying length NARS with the corresponding standard deviation shown in whiskers from observations (in gray) and historical simulations simulation of the CMIP6 models. The whiskers indicate the corresponding standard deviation.

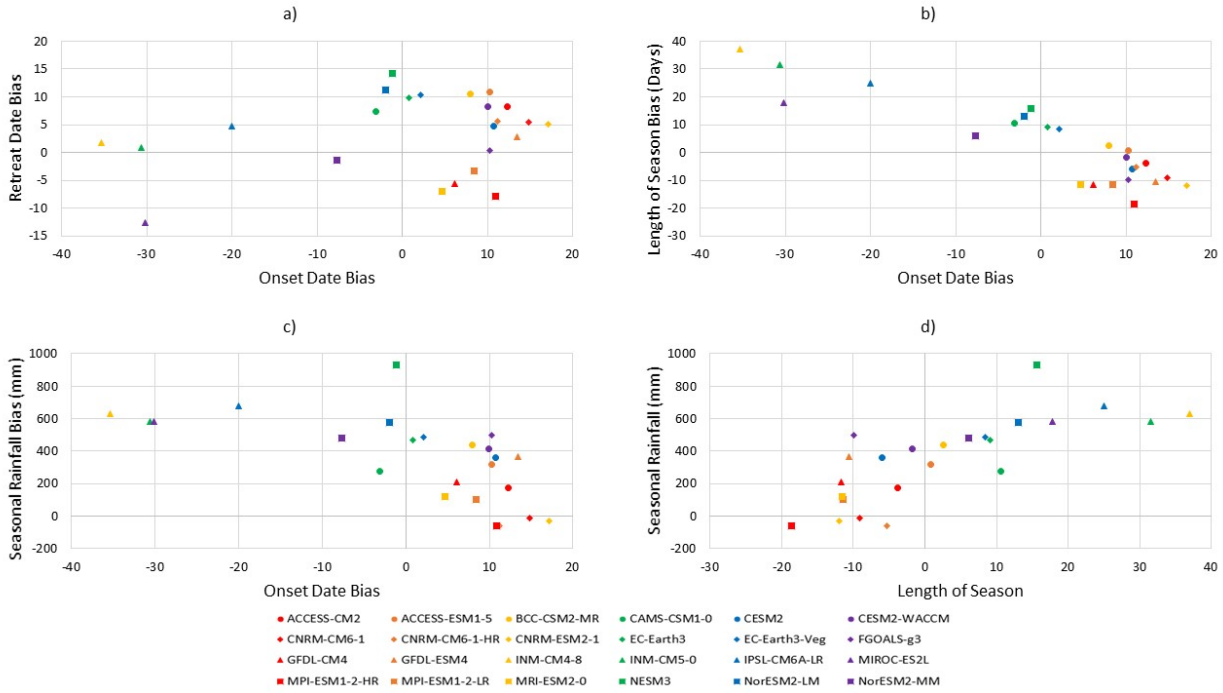

Figure 20: The scatter of the climatological bias of onset date of NARS with corresponding climatological bias of a) demise date, b) length of season, and c) seasonal rainfall from the historical simulation of the CMIP6 models. d) Similarly, the scatter of the climatological seasonal rainfall bias of NARS with corresponding climatological bias of the length of the season from the historical simulation of the CMIP6 models.

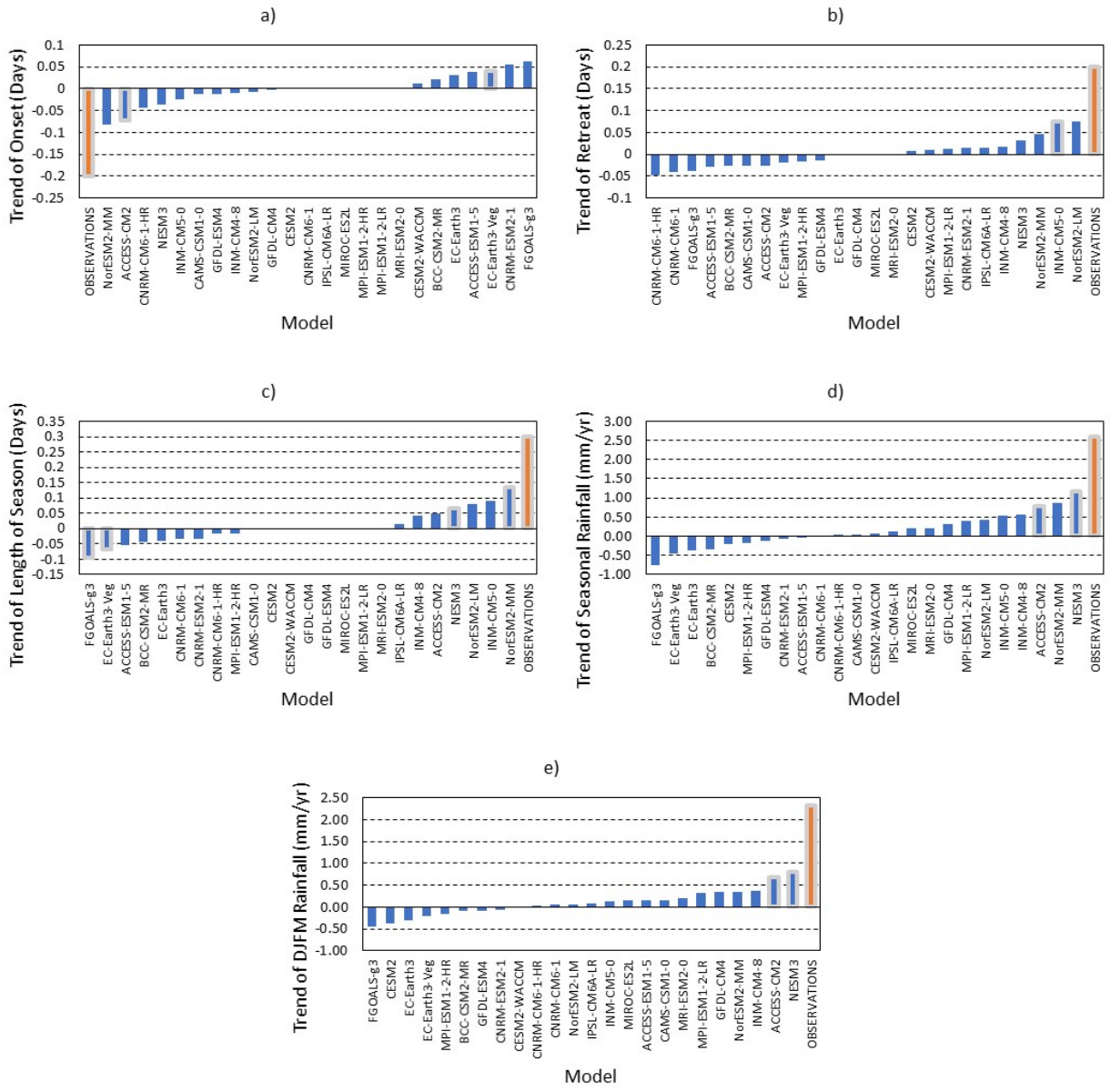

Figure 21: The linear trends (days yr^{-1}) of the a) onset date, b) demise date, and c) length of NARS from the historical simulations of CMIP6 models and observations. Similarly, the linear trends (mm yr^{-1}) of seasonal rainfall with d) varying seasonal length and e) fixed length (December-January-February) NARS from the historical simulation of CMIP6 models and observations. All the linear trends that pass the Mann-Kendall statistical significance test at 99% confidence interval are shown with gray outline.

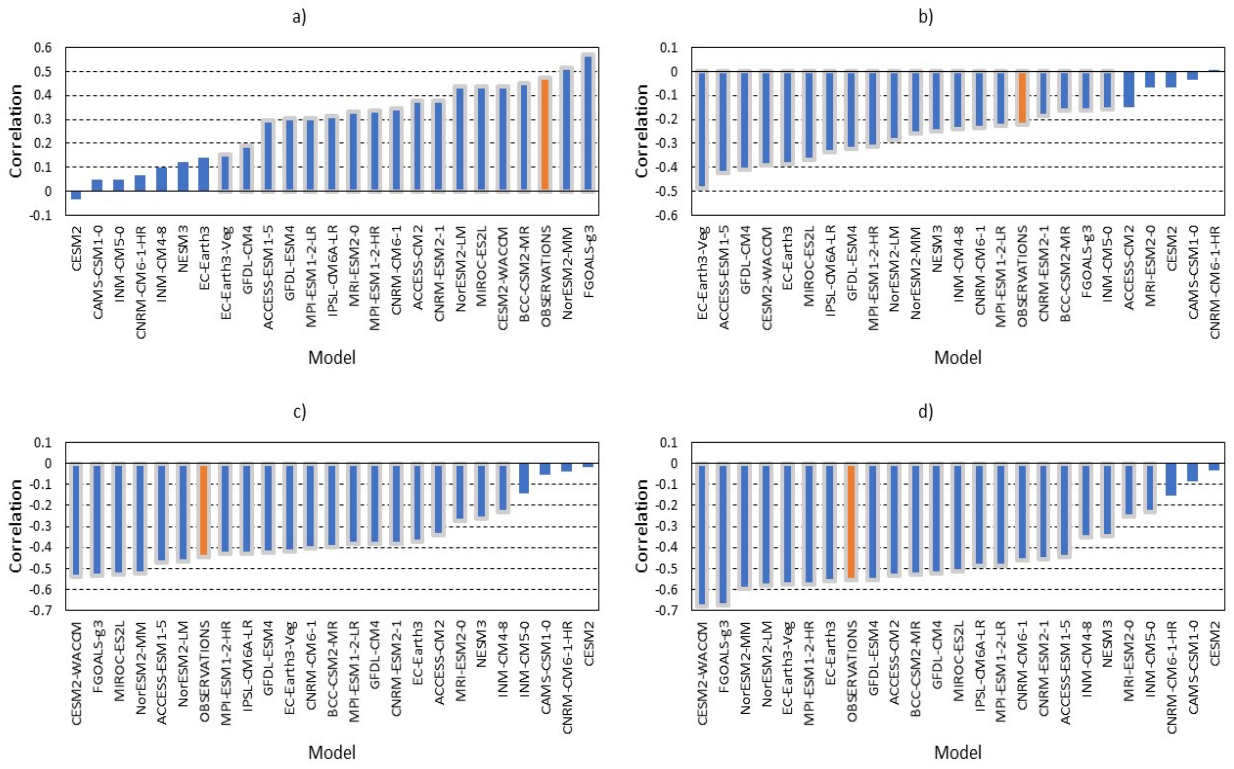

Figure 22: The correlations of the anomalies after removing the linear trend of a) onset date, b) retreat date, c) seasonal length, d) seasonal rainfall anomaly of NARS with corresponding seasonal mean December-January-February (DJF) anomaly of SST over the Niño3.4 region from the historical simulation of CMIP6 models and observations. The linear trend in the SST is also removed. Anomaly correlations that are statistically significant values at 95% confidence interval are shaded with gray outline.

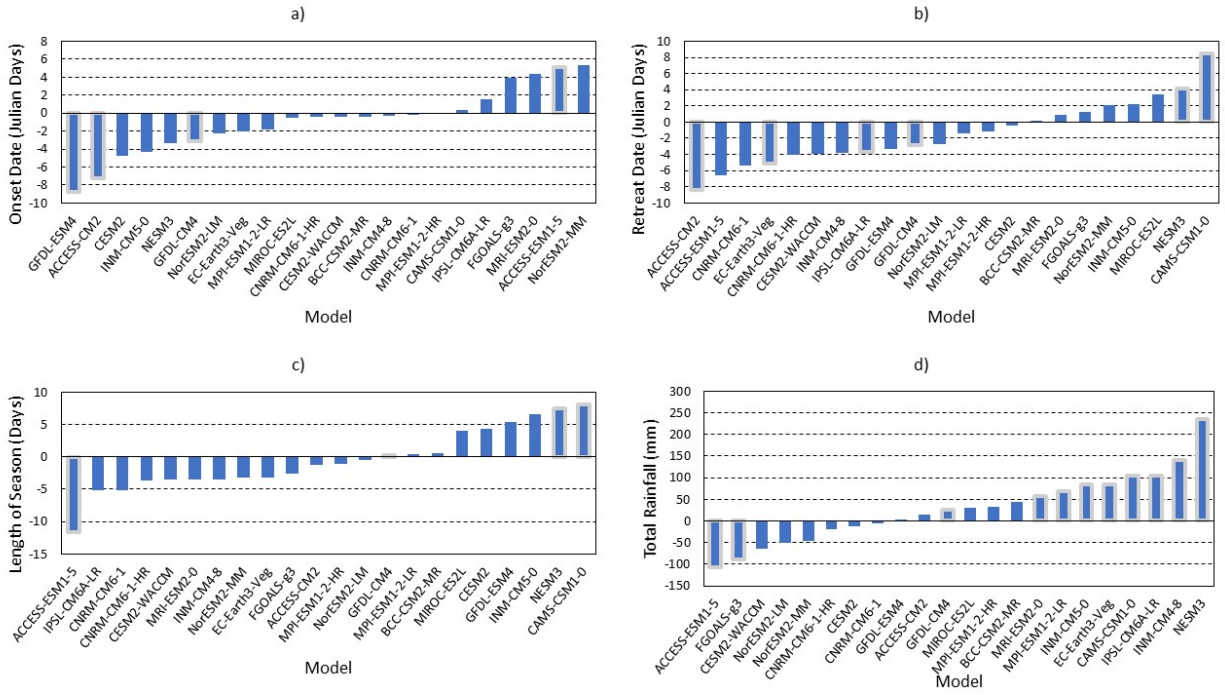

Figure 23: The climatological change with respect to the historical simulations in (a) onset date (days), (b) retreat date (days), (c) the length (days), (d) seasonal rainfall (mm) with varying length of NARS with the corresponding standard deviation shown in whiskers from SSP585 simulation of the CMIP6 models. The change that is statistically significant at 95% significance level is outlined in gray.

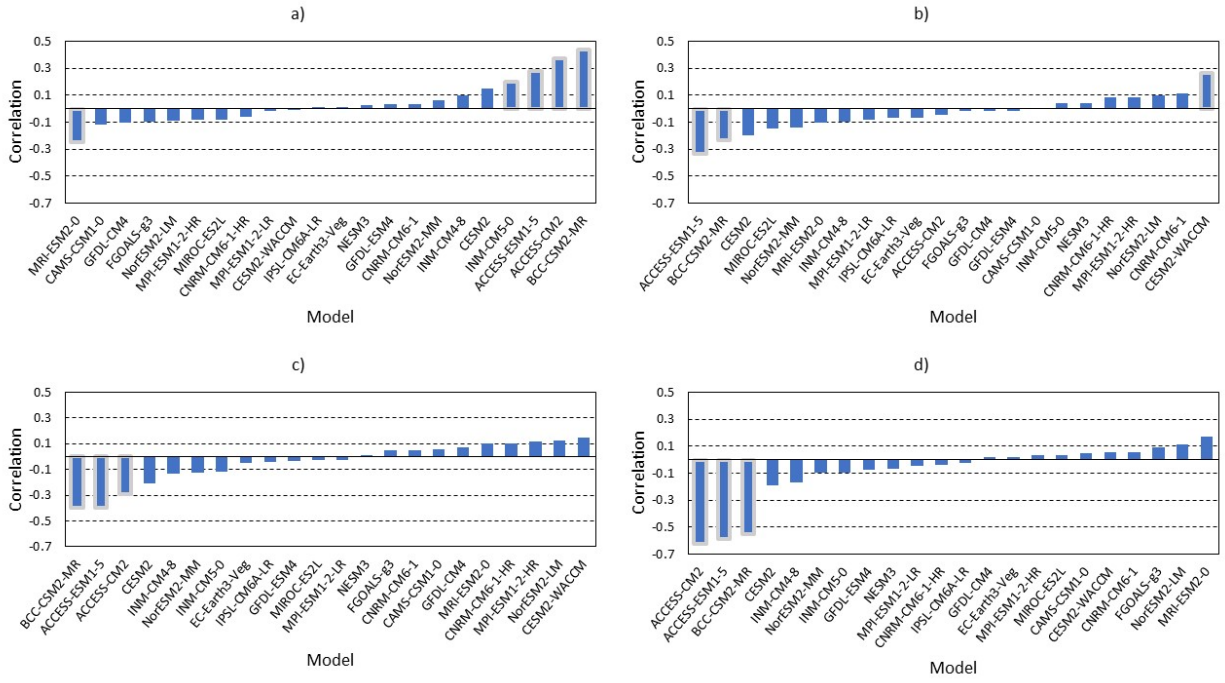

Figure 24: The correlations of the anomalies after the linear trend is removed of a) onset date, b) retreat date, c) seasonal length, d) seasonal rainfall anomaly with varying length of NARS with corresponding seasonal mean December-January-February mean anomaly of SST over the Niño3.4 region from the SSP585 simulation of the CMIP6 models. The linear trend in the SST is also removed. The correlations that are significant at 95% confidence interval are shaded in gray.

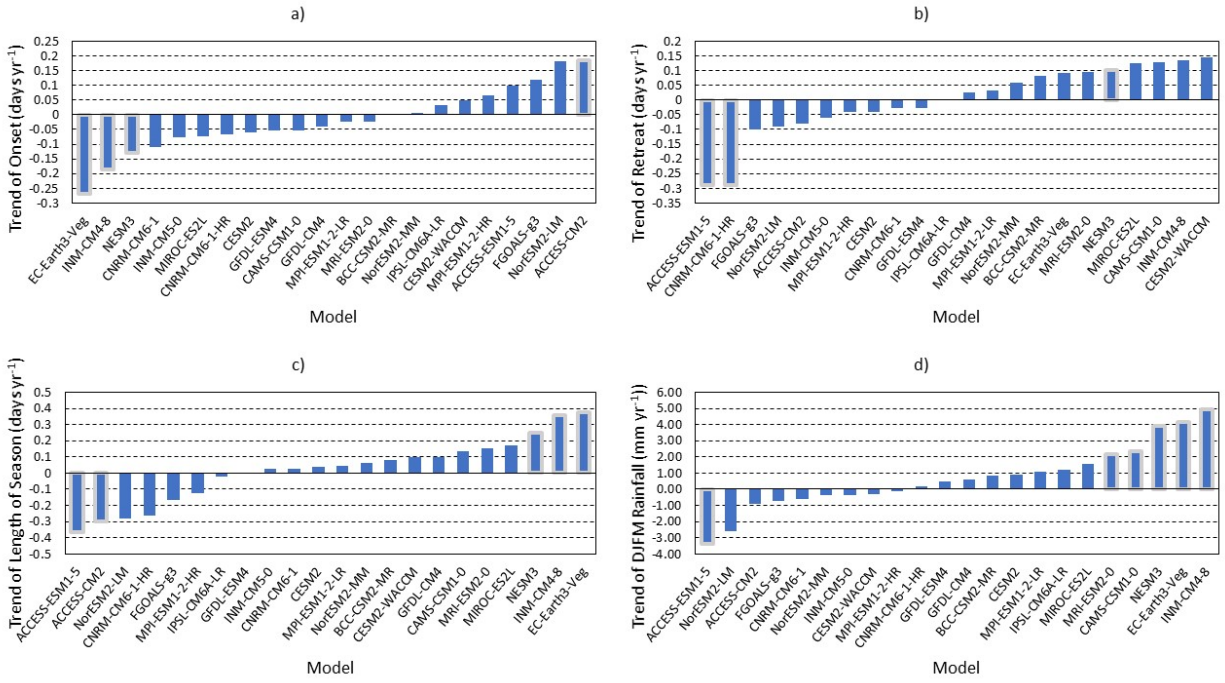

Figure 25: The linear trends (days yr^{-1}) of the a) onset date, b) demise date, and c) length of NARS from the SSP585 simulation of CMIP6 models. d) Similarly, the linear trends (mm yr^{-1}) of seasonal rainfall with varying seasonal length of NARS from the SSP585 simulation of CMIP6 models. All the linear trends that pass the Mann-Kendall statistical significance test at 95% confidence interval are shown in gray.

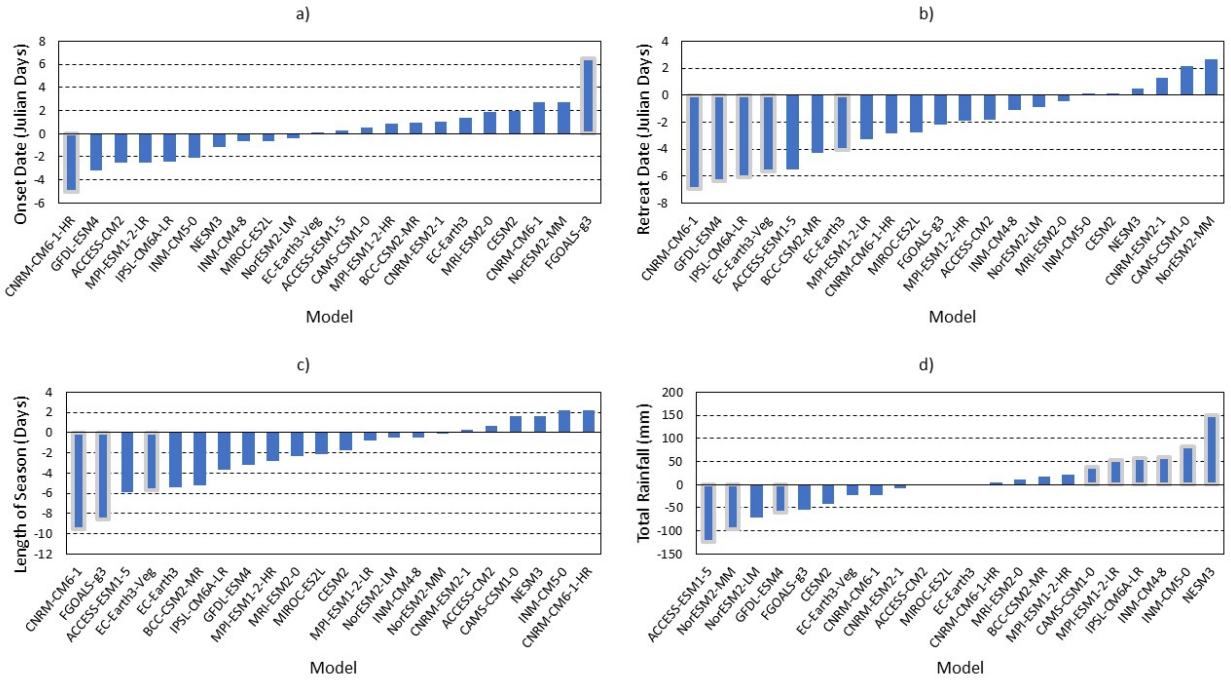

Figure 26: The climatological change with respect to the historical simulations in (a) onset date (in days), (b) retreat date (in days), (c) the length (in days), (d) seasonal rainfall with varying length, and (e) seasonal rainfall with fixed length (December-January-February) season of NARS with the corresponding standard deviation shown in whiskers from SSP126 simulation of the CMIP6 models. The change that is statistically significant at 95% significance level is outlined in gray.

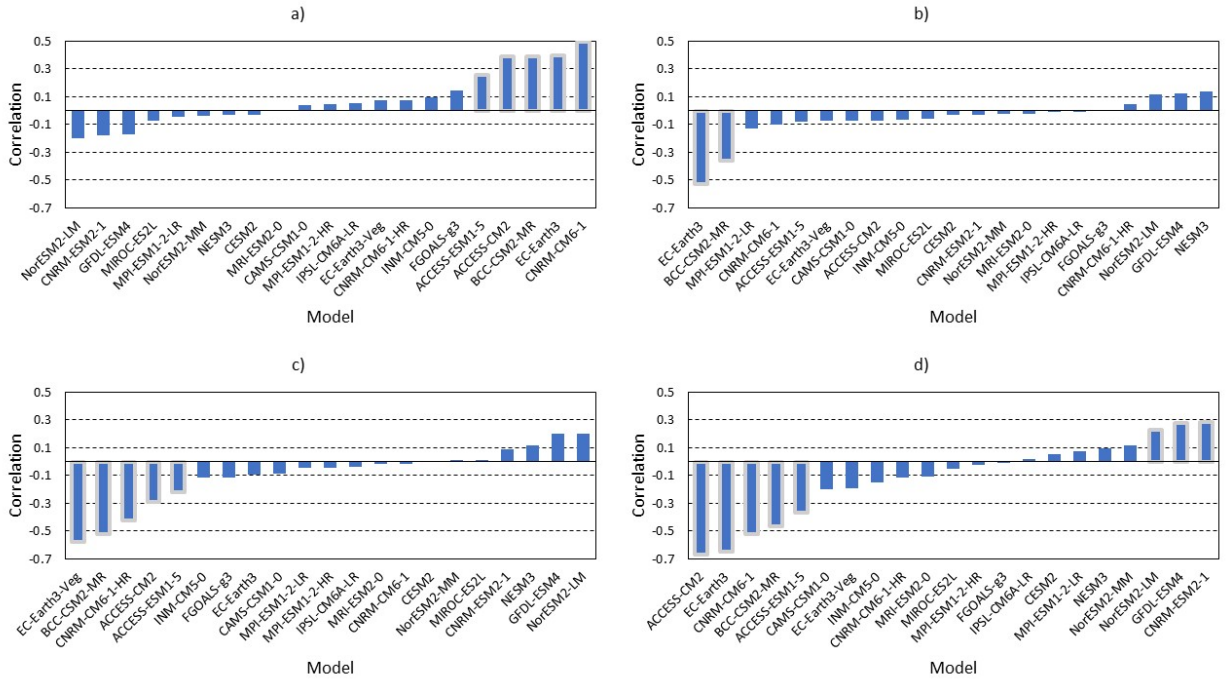

Figure 27: The correlations of the anomalies after the linear trend is removed of a) onset date, b) retreat date, c) seasonal length, d) seasonal rainfall anomaly with varying length of NARS with corresponding seasonal mean December-January-February mean anomaly of SST over the Niño3.4 region from the SSP126 simulation of the CMIP6 models. The linear trend in the SST is also removed. The correlations that are significant at 95% confidence interval are outlined in gray.

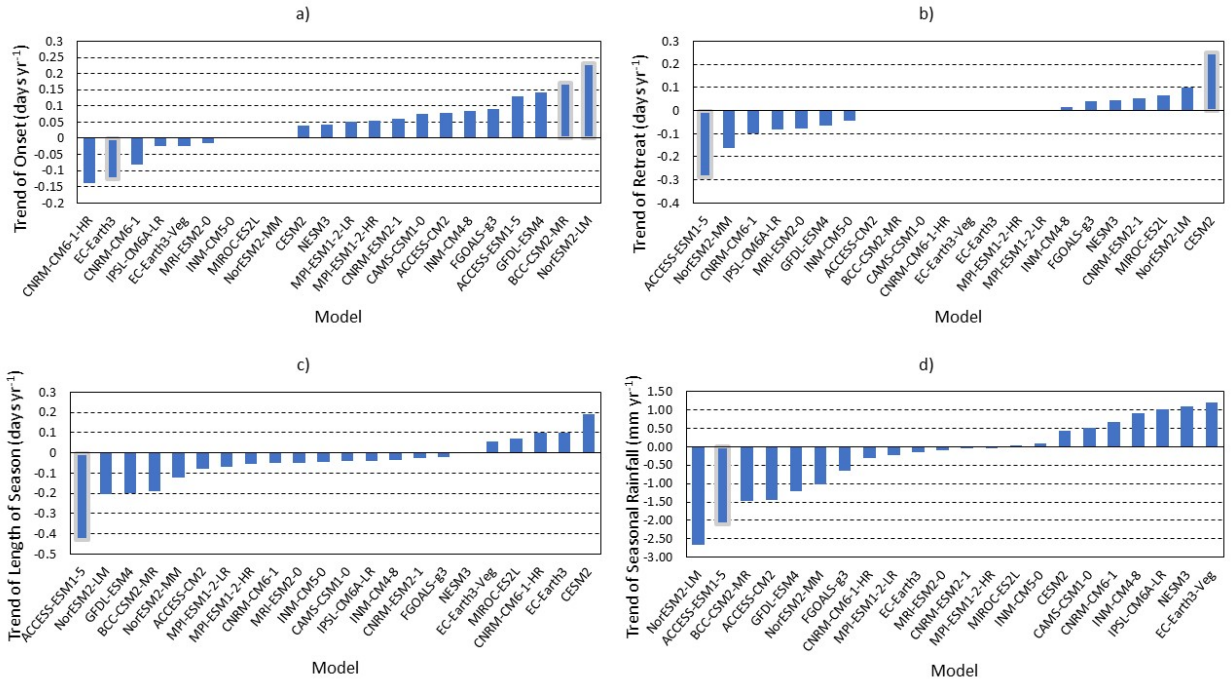

Figure 28: The linear trends (days yr^{-1}) of the a) onset date, b) demise date, and c) length of NARS from the SSP126 simulation of CMIP6 models. d) Similarly, the linear trends (mm yr^{-1}) of seasonal rainfall with varying seasonal length of NARS from the SSP126 simulation of CMIP6 models. All the linear trends that pass the Mann-Kendall statistical significance test at 95% confidence interval are outlined in gray.

REFERENCES

Beobide-Arsuaga, H., T. Bayr, A. Reintges, and M. Latif, 2021: Uncertainty of ENSO-amplitude projections in CMIP5 and CMIP6 models. Clim. Dyn., 56, 3875-3888.

Brown, J. R., Brierley, C. M., An, S.-I., Guarino, M.-V., Stevenson, S., Williams, C. J. R., Zhang, Q., Zhao, A., Abe-Ouchi, A., Braconnot, P., Brady, E. C., Chandan, D., D'Agostino, R., Guo, C., LeGrande, A. N., Lohmann, G., Morozova, P. A., Ohgaito, R., O'ishi, R., … Zheng, W. (2020). Comparison Of Past And Future Simulations Of ENSO In CMIP5/PMIP3 And CMIP6/PMIP4 Models. Climate Of The Past, 16(5), 1777–1805. Https://Doi.Org/10.5194/Cp-16-1777-2020.Chen, Z., Zhou, T., Zhang, L., Chen, X., Zhang, W., & Jiang, J. (2020). Global land monsoon precipitation changes in CMIP6 projections. Geophysical Research Letters, 47(14), e2019GL086902. https://doi.org/10.1029/2019gl086902

Di Luca, A., Pitman, A. J., & de Elía, R. (2020). Decomposing temperature extremes errors in CMIP5 and CMIP6 models. Geophysical Research Letters, 47(14), 1– 10. https://doi.org/10.1029/2020gl088031

Drosdowsky W. 1996. Variability of the Australian summer monsoon at Darwin: 1957–1992. J. Climate 9: 85–96.

ElNesr, M. N., M. M. Abu-Zreig, and A. A. Alazba, 2010: Temperature trends and distribution in the Arabian Peninsula. Am. J. Environ. Sci., 6, 191-203, doi:10.3844/ajessp.2010.191.203.

Eyring, V., Bony, S., Meehl, G. A., Senior, C. A., Stevens, B., Stouffer, R. J., & Taylor, K. E. (2016). Overview of the Coupled Model Intercomparison Project Phase 6 (CMIP6) experimental design and organization. Geoscientific Model Development, 9(5), 1937–1958. https://doi.org/10.5194/gmd-9-1937-2016.

Forster, P. M., Maycock, A. C., McKenna, C. M., & Smith, C. J. (2020). Latest climate models confirm need for urgent mitigation. Nature Climate Change, 10, 7– 10.

Fredriksen, H. B., J. Berner, A. C. Subramanian, and A. Capotondi, 2020: How does El Niño-Southern Oscillation change under greenhouse gas warming-A first look at CMIP6, Geophys. Res. Lett., https://doi.org/10.1029/2020GL090640.

Gettelman, A., Hannay, C., Bacmeister, J. T., Neale, R. B., Pendergrass, A. G., Danabasoglu, G., et al. (2019). High climate sensitivity in the Community Earth System Model Version 2 (CESM2). Geophysical Research Letters, 46, 8329–8337. https://doi.org/10.1029/2019GL083978.

Ghil, M., M. Allen, M. Dettinger, K. Ide, D. Kondrashov, M. Mann, A. W. Robertson, A. Saunders, Y. Tian, F. Varadi, and coauthors, 2002: Advanced spectral methods for climatic time series. Rev Geophys 40(1):31– 341. https://doi.org/10.1029/2000RG000092

Grant, I., 2012: Daily Rain Gauge Precipitation (Rainfall) - Gridded, Australia coverage. Available from http://data.auscover.org.au/xwiki/bin/view/Product+pages/Product+User+Page+Melbourne+2

Grose, M. R., Narsey, S., Delage, F. P., Dowdy, A. J., Bador, M., Boschat, G., & Power, S. (2020). Insights from CMIP6 for Australia's future climate. Earth's Future, 8(5), e2019EF001469. https://doi.org/10.1029/2019ef001469

Gusain, A., Ghosh, S., & Karmakar, S. (2020). Added value of CMIP6 over CMIP5 models in simulating Indian summer monsoon rainfall. Atmospheric Research, 232, 104680. https://doi.org/10.1016/j.atmosres.2019.104680

Hendon, H. H. and B. Liebmann, 1990a: A composite study of onset of the Australian summer monsoon. Journal of the Atmospheric Sciences 47: 2227–2240.

Hendon, H. H. and B. Liebmann, 1990b: The intraseasonal (30–50 day) oscillation of the Australian summer monsoon. Journal of the Atmospheric Sciences 47: 2909–2924.

Hendon, H. H., N. E. Davidson, and B. Gunn, 1989: Australian summer monsoon onset during AMEX 1987. Monthly Weather Review 117: 370–390.

Holland G. J., 1986: Interannual variability of the Australian summer monsoon at Darwin: 1952-82. Monthly Weather Review 144: 594–604.

Jassby, A. D., and J. E. Cloern, 2015: wq: Exploring water quality monitoring data, version 0.4.3, http://cran.r-project.org/web/packages/wq/index.html.

Jones D.A., Wang W., Fawcett R. (2009) High-quality spatial climate datasets for Australia. Australian Meteorological and Oceanographic Journal 58, 233-248.

Karmakar, N., A. Chakraborty, R. S. Nanjundiah, 2017: Space-time evolution of the low- and high-frequency intraseasonal modes of the Indian Summer Monsoon. Mon Weather Rev 145(2):413–435. https://doi.org/10.1175/MWR-D-16-0075.1.

Karmakar, N. and V. Misra, 2019: The fidelity of a regional coupled model in capturing the relationship between intraseasonal variability and the onset/demise of the Indian summer monsoon. Clim. Dyn., https://doi.org/10.1007/s00382-020-05252-z.

Krishnamurti, T. N., S. K. Han, and V. Misra, 1995: Predictions of dry and wet spells of the Australian Monsoon. Int. J. Climatol., 15, 753-771.

Lin, Z., & Li, Y. (2012). Remote influence of the tropical Atlantic on the variability and trend in north West Australia summer rainfall. Journal of Climate, 25, 2408–2420. https://doi.org/10.1175/jcli-d-11-00020.1.

Lisonbee, J., J. Ribbe, and M. Wheeler, 2020: Defining the north Australian monsoon onset: A systematic review. Prog. Phys. Geog., 1-21, doi:10.1177/0309133319881107.

Lo, F. and M. C. Wheeler, 2007: Probabilistic forecasts of the onset of the North Australian wet season. Mon. Wea. Rev., 135, 3506-3520.

Meals, D. W., J. Spooner, S. A. Dressing, and J. B. Harcum, 2011: Statistical analysis of monotonic trends. Tech Notes 6, Tetra Tech, U. S. Environmental Protection Agency, Fairfax, VA, 23 pp., Available from: https://www.epa.gov/sites/default/files/2016-05/documents/tech_notes_6_dec2013_trend.pdf

Meinshausen, M., Nicholls, Z., Lewis, J., Gidden,M. J., Vogel, E., Freund, M., et al. (2019). The SSP greenhouse gas concentrations and their extensions to 2500. Geoscientific Model Development Discussion, 2019, 1–77. https://doi.org/10.5194/gmd-2019-222.

Misra, V., A. Mishra, and A. Bhardwaj, 2017a: Local onset and demise of the Indian summer monsoon. Clim. Dyn., 51, 1609-1622, doi:10.1007/s00382-017-3924-2.

Misra, V., A. Bhardwaj, and R. Noska, 2017b: Understanding the variations of the length and the seasonal rainfall anomalies of the Indian summer monsoon. J. Climate, 30, 1753-1763.

Mo, K. C., 2010: Interdecadal modulation of the impact of ENSO on precipitation and temperature over the United States. J. Climate, 23, 3639–3656, doi:10.1175/ 2010JCLI3553.1.

Narsey, S. Y., J. R. Brown, R. A. Colman, F. Delage, S. B. Power, A. F. Moise, and H. Zhang, 2020: Climate change projections for the Australian monsoon from CMIP6 models. Geophys. Res. Lett., https://doi.org/10.1029/2019GL086816.

NCC-Editorial (2019). The CMIP6 landscape. Nature Climate Change, 9, 727–727.

Nicholls N, McBride JL, Ormerod RJ. 1982. On predicting the onset of the Australian wet season at Darwin. Monthly Weather Review 110: 14–17.

Nicholls, N., 1984: A system for predicting the onset of the north Australian wet season. J. Climatol., 4, 425-436.

Partal, T. and E. Kahya, 2006: Trend analysis in Turkish precipitation data. Hydrol. Processes, 20, 2011-2026, doi:10.1002/hyp.5993.

Pope, M., C. Jakob, and M. J. Reeder, 2009: Regimes of the north Australian wet season. J. Climatol., 22, 6699-6715.

Randall, D. A., Wood, R. A., Bony, S., Colman, R., Fichefet, T., Fyfe, J., et al. (2007). Climate models and their evaluation. In Climate change 2007: The physical science basis. Contribution of working group I to the fourth assessment report of the IPCC (FAR) (pp. 589– 662). Cambridge University Press.

Ridder, N. N., Pitman, A. J., & Ukkola, A. M. (2021). Do CMIP6 Climate Models Simulate Global Or Regional Compound Events Skillfully? Geophysical Research Letters, 48(2). Https://Doi.Org/10.1029/2020GL091152.

Sen, P. K., 1968: Estimates of the regression coefficient based on Kendall's tau. J. Am. Stat. Assoc., 63, 1379-1389.

Smith, I. N., L. Wilson, and R. Suppiah, 2008a: Characteristics of the Northern Australian Rainy Season. J. Climate, 21, 4298-4311.

Smith, T. M., R. W. Reynolds, T. C. Peterson, J. Lawrimore, 2008b: Improvements to NOAA's historical merged land-ocean surface temperature analysis (1880-2006). J. Climate, 21, 2283-2296.

Sherwood, S. C., Webb, M. J., Annan, J. D., Armour, K. C., Forster, P. M., Hargreaves, J. C., et al. (2020). An assessment of Earth's climate sensitivity using multiple lines of evidence. Reviews of Geophysics, 58, e2019RG000678. https://doi.org/10.1029/2019RG000678

Shukla, J., T. DelSole, M. Fennessy, J. Kinter, and D. Paolino, 2006: Climate Model Fidelity and Projections of Climate Change. Geophys. Res. Lett., 33, L07702, doi:10.1029/2005GL025579.

Taylor, K. E., Stouffer, R. J., & Meehl, G. A. (2012). An overview of CMIP5 and the experiment design. Bulletin of the American Meteorological Society, 93(4), 485–498. https://doi.org/10.1175/BAMS-D-11-00094.1.

Troup A. J., 1961: Variations in upper tropospheric flow associated with the onset of the Australian monsoon. Indian Journal of Meteorology and Geophysics 12: 217–230.

Uehling, J. and V, Misra, 2020: Characterizing the Seasonal Cycle of the Northern Australian Rainy Season. J. Climate, 33 (20): 8957–8973.

van Vuuren, D., Edmonds, J., Kainuma, M., Riahi, K., Thomson, A., Hibbard, K., et al. (2011). The representative concentration pathways: An overview. Climatic Change, 109(1-2), 5–31. https://doi.org/10.1007/s10584-011-0148-z.

Voosen, P. (2019). New climate models predict a warming surge. Science News. https://doi.org/10.1126/science.aax7217

Wilks, D. S., 2011: Statistical Methods in the Atmospheric Sciences. 3rd ed. International Geophysics Series, Vol. 100, Academic Press, 676 pp.

Wheeler, M. C. and H. H. Hendon, 2004: An all-season realtime multivariate MJO index: Development of an index for monitoring and prediction. Monthly Weather Review 132: 1917–1932

Wheeler, M. C. and J. L. McBride, 2012: Australasian monsoon. In: Lau WKM and Waliser DE (eds) Intraseasonal Variability in the Atmosphere–Ocean Climate System. 2nd ed., Berlin Heidelberg: Springer-Verlag, pp. 147–197.

Xu, S. X., K. Takeuchi, and H. Ishidaira, 2003: Monotonic trend and step changes in Japanese precipitation. J. Hydrol., 279, 144-150, doi:10.1016/s0022-1694(03)00178-1.

Yuan, J., W. Li, and Y. Deng, 2015: Amplified subtropical stationary waves in boreal summer and their implications for regional water extremes. Environ. Res. Lett., 10, 104009, doi:10.1088/1748-9326/10/10/104009.

Zelinka, M. D., Myers, T. A., McCoy, D. T., Po-Chedley, S., Caldwell, P. M., Ceppi, P., Klein, S. A., & Taylor, K. E. (2020). Causes of higher climate sensitivity in CMIP6 models. Geophysical Research Letters, 47, e2019GL085782. https://doi.org/10.1029/2019GL085782

Zhang, C. (2013). MADDEN–JULIAN OSCILLATION: Bridging Weather And Climate. Bulletin Of The American Meteorological Society, 94(12), 1849–1870. Https://Doi.Org/10.1175/BAMS-D-12-00026.1

BIOGRAPHICAL SKETCH

Objective

Seeking to continue to pursue a research focused career in the field of meteorology after completing my Ph.D., while expanding my knowledge and skillset.

Experience

Teaching Assistant

Florida State University, Tallahassee, FL

August 2017 – May 2019

As a teaching assistant at Florida State, I had the responsibilities of grading student assignments and tests for multiple courses. Additionally, I was responsible for helping undergraduate students when they were completing assignments or studying for exams. As a teaching assistant I was nominated for the Outstanding Teaching Assistant award.

Research Assistant

Florida State University, Tallahassee, FL

August 2019– December 2021

As a research assistant, I worked towards the completion of multiple research projects associated with my Ph.D. in meteorology. These research projects have led to published peer-reviewed papers.

Education

Bachelor of Science in Meteorology

University of Oklahoma, Norman, OK

December 2016

Received a 3.5 GPA and hold minors in both mathematics and geography and achieved the Dean's list.

Master of Science in Meteorology

Florida State University, Tallahassee, FL

August 2019

Received a 3.6 GPA and received departmental award for academic performance.

Doctor of Philosophy in Meteorology
Florida State University, Tallahassee, FL
Intended graduation - December 2021
Received a 3.6 GPA while taking courses with a focus on tropical, synoptic, and physical meteorology. Additionally completed numerous research projects with a focus on monsoons and CMIP climate models.

Skills

Public speaking
Computing – Very comfortable using both Windows and MacOS, with strong skills in Microsoft software (Excel, Word, Powerpoint).
Programming – Performed tasks in numerous computer programming languages including Fortran, GrADS, Matlab, and Python.
Statistical data analysis and mathematics
Problem Solving
Flexible, reliable, dependable, with strong leadership skills

Leadership

Held the position of treasurer for the Thalassic Society at Florida State University
Eagle Scout rank achieved

Publications

Uehling, J. and V. Misra 2020: Characterizing the seasonal cycle of the Northern Australian Rainy Season
Works currently in peer-review:
Uehling, J. et al. 2021: Characterizing the Local Variations of the Northern Australian Rainy Season
Uehling, J and V. Misra 2021: Australia's rainy season in a future climate